



Dual modulation on peroxyomonosulfate activation site and photocarrier separation in carbon nitride for efficient photocatalytic organics degradation: Efficacy and mechanism evaluation

Rongdi Tang ^{a,b}, Hao Zeng ^b, Yaocheng Deng ^{b,*}, Sheng Xiong ^b, Ling Li ^b, Zhanpeng Zhou ^b, Jiajia Wang ^{a,*}, Lin Tang ^a

^a College of Environmental Science and Engineering, Hunan University and Key Laboratory of Environmental Biology and Pollution Control (Hunan University), Ministry of Education, Changsha 410082, PR China

^b College of Environment and Ecology, Hunan Agricultural University, Changsha 410128, PR China



ARTICLE INFO

Keywords:

Peroxyomonosulfate
Photodegradation
Polymeric carbon nitride
Dual modulation
Water treatment

ABSTRACT

Herein, sulfur and sodium co-doped cyano-rich polymeric carbon nitride (NaCNS) have been designed to boost photocatalytic atrazine (ATZ) degradation with peroxyomonosulfate (PMS) assistance. The NaCNS was fabricated via a two-step thermal condensation with the existence of sodium chloride and cysteine, and the ATZ degradation in the system was evaluated via batch experiments. Compared to pristine carbon nitride, the reaction rate constant of NaCNS was dramatically enhanced nearly sixfold ($47.66 \times 10^{-3} \cdot \text{min}^{-1}$). Given the experiments and theoretical calculation, the ATZ degradation in the system was mainly dominated by the electrophilic attack of $^1\text{O}_2$, leading to the production of 11 intermediates with reduced ecotoxicity. The promoted photocatalytic performance was originating from the dual modulation of NaCNS, where the sodium act as a PMS activation site while the cyano and sulfur construct an electronic push-pull system for better photocarrier separation. Hopefully, this study can inspire the rational design of catalysts for efficient photocatalytic PMS activation.

1. Introduction

Atrazine (ATZ) is a widely applied herbicide in crop production to control grassy and broadleaf weeds. [1,2]. Given its low price and effectiveness for weeding, the annual global consumption of ATZ reaches 70–90 thousand tons [3]. However, atrazine is physically and chemically stable, which is difficult to be degraded naturally or biodegraded by microorganisms [4,5]. In 2003, the use of ATZ has been banned in Europe, but its residue detected in Paris in 2019 still reach 255–787 ng/L [6,7]. The abuse of ATZ has threatened the health of the ecosystem. Though ATZ is not acutely toxic to people, it may still induce tumors and cancer in the human body of its character as an endocrine disruptor [8]. Therefore, it is necessary to control the ATZ residue and minimize its negative effect on the ecosystem and human beings. So far, many technologies including adsorption [9], biodegradation [1,10], and photocatalysis have been applied for ATZ control [11–13]. Given the potential of solar conversion and the distinct effect on contaminant decomposition, visible-light-driven photocatalysis has been considered one of the most promising environmentally friendly technology for

removing organic contaminants in water [13,14]. The photogenerated electrons and holes, as well as the reactive oxygen species (ROS) generated during photocatalysis, can effectually degrade organics by destroying the chemical bonds [15,16]. While limited by the intrinsic high recombination rate of photoexcited electrons and holes, the photodegradation efficiency for refractory pollutant ATZ is still restricted [17,18]. Therefore, coupling photocatalysis with other strategies to enhance the catalytic efficiency is essential to make a breakthrough in ATZ elimination.

Establishing a high-efficient catalytic system via coupling photocatalysis with the oxidant peroxyomonosulfate (PMS) is likely to produce more ROS [19,20]. Upon activation during photocatalysis, PMS can serve as an electron acceptor in the system [21]. In this way, the consumption of electrons would therefore decrease the recombination rate of the photogenerated electrons and holes. Meanwhile, the PMS can be activated and generate ROS such as $\cdot\text{SO}_4^-$, $\cdot\text{O}_2^-$, $^1\text{O}_2$, and $\cdot\text{OH}$ to achieve the synergistic effect during the photocatalytic PMS activation process for high-efficient organics degradation [16,22]. In such a system, the

* Corresponding authors.

E-mail addresses: dengyaocheng@hunau.edu.cn (Y. Deng), wangjiajia07@hnu.edu.cn (J. Wang), tanglin@hnu.edu.cn (L. Tang).

catalyst plays the role of a cornerstone in reducing the kinetic energy barrier of the reaction. To achieve potential practical application, ideal catalysts for the photocatalytic PMS activation should have a suitable electronic band structure with good redox capacity and allows effective generation of photocarriers. Besides, the economic cost of photocatalysts is also another important factor. As a metal-free organic semiconductor consisting of earth-abundant elements, polymeric carbon nitride (PCN) and its derivatives with suitable bandgap (2.7 eV) has aroused the wild attention of researchers in the photocatalysis field [13, 23–25]. Besides, PCN has been reported high activity in $^1\text{O}_2$ -dominated non-radical degradation for contaminants, which shows great resistance to coexisting substances [26,27].

However, the photocatalytic performance and PMS activation ability of the pristine PCN are limited. Therefore, rational design and modification of PCN are necessary for high-efficient water treatment. In terms of photocatalysts, the separation of the photogenerated electrons and holes is the fundamental factor, which can be modulated by adjusting the electronic configuration in the catalyst. In previous research, whether it is the construction of heterojunction [25,28], element doping [29,30], or molecular modification [31,32], the core of catalyst modification is to adjust the electron distribution and trigger an effective separation of photogenerated electrons and holes. Our previous study has successfully constructed a donor- π -acceptor electronic structure in PCN via bimolecular modification, achieving the rearrangement of the electron-rich region and electron-depletion region in the catalyst and greatly decreasing the recombination of photogenerated electrons and holes [33]. Similarly, Wang et al. introduced Cu-N₄ and C-S-C in PCN, respectively acting as electronic receptors and donors to facilitate the separation of photocarriers [34]. Therefore, proper modification of PCN by introducing electron acceptor and electron donor components can promote photocatalytic performance. In terms of PMS activation, how to improve the effective mass transfer between catalyst and PMS, boosting the ROS generation is the key issue lied to researchers. So far, many researchers have tried to achieve better mass transfer between the catalyst and PMS by rational regulation of the catalyst [27,35,36]. While within our knowledge, there are more studies focused on the transformation process of PMS in the system, ignoring the realization of effective interaction between PMS and catalyst via equipping a precise activation site on the catalyst. Given that PMS is a Lewis acid that easily interacts with Lewis base [37–39], and the metal can act as an electron channel between the PMS and catalyst to facilitate the electron transfer [34], introducing low-cost Lewis alkali metal into the catalyst is likely to improve PMS activation efficiency from the aspect of their effective interaction. Thus, the dual modulation on PCN to establish an electronic push-pull system with electron donor and receptor, while introducing an accessible alkali metal acting as Lewis base can achieve efficient photocarrier separation and PMS activation for effective ATZ degradation.

Inspired by previous research, this study aims to reasonably design the sulfur and sodium co-doped cyano-rich polymeric carbon nitride (NaCNS), realizing the dual modulation on the PMS activation site and the directional photocarrier separation of PCN. The sodium dopant can attract the PMS molecule via Lewis acid-base interaction, facilitating the mass transfer in the photocatalytic PMS activation system. Meanwhile, the sulfur dopant and the cyano groups (a type of nitrogen vacancies) in the PCN framework can respectively act as electron donors and acceptors to construct an electronic push-pull system, facilitating the directional movement of photogenerated electrons and holes [39–42]. The chemical composition and electronic configuration of NaCNS were characterized and analyzed via density functional theory (DFT) calculation; the ATZ degradation with different environmental factor interference was evaluated via batch experiments; the photocatalytic mechanism and the ATZ degradation mechanism was experimentally and theoretically assessed via analyzing the PMS activation, the electron transfer, the ROS transformation, and the ATZ degradation processes. This study is expected to provide a dual modulation strategy of catalyst

for the high-efficient elimination of organics in a photocatalytic PMS activation system.

2. Experimental section

2.1. Characterization

The microstructure and the morphology of the photocatalysts were investigated by scanning electron microscopy (SEM, Tescan MIRA LMS, 5k eV scanning voltage), and transmission electron microscopy (TEM, FEI Titan G2 60–300). The crystal structure of the photocatalysts was measured via X-ray diffraction (XRD, Rigaku Miniflex 600, 10°/min scanning rate). The chemical composition and the functional groups in the catalysts were investigated via Fourier transforms infrared spectrometer (FT-IR, Thermo Nicolet iN10), X-ray photoelectron spectra (XPS, Thermo Scientific K-Alpha), and Solid state nuclear magnetic resonance (SSNMR, Bruker 600 M). The light response of catalysts was assessed via ultraviolet-visible diffused reflectance spectra (UV-vis DRS, Shimazu UV-3600 plus) U4100. The separation and recombination of photocarrier in photocatalysts were tested via photoluminescence emission spectroscopy (PL, fluorescence spectrometer, Hitachi, F-700). The generated reactive species during the photocatalysis were detected via electron spin resonance spectra (ESR, Bruker -EMXPlus-10/12).

2.2. Photoelectrochemical analysis

The photoelectrochemical property of the catalysts was measured by linear sweep voltammetry (LSV), electrochemical impedance spectroscopy (EIS), and photocurrent response curve via the CHI 660E workstation. The photoelectrochemical analysis was conducted in 0.2 M Na₂SO₄ electrolyte solution with a three-electrode model, including an Ag/AgCl electrode, a Pt electrode, and a working electrode. During the assessment, the applied light condition was the same as the photocatalysis. The working electrode was prepared by catalysis. Typically, 10 mg catalyst, 1 mL ethanol, and 1 mL 0.5% Nafion solution were evenly mixed with an ultrasonic cleaner. Then, 200 μL suspension was dropped on a 1 cm \times 2 cm FTO slice with a half-effective working area.

2.3. Density functional theory calculations

The density functional theory calculations DFT were carried out via Vienna Ab-initio Simulation Package (VASP) to investigate the electronic structure change on photocatalysts. The molecular geometric optimization was conducted by projected augmented wave (PAW) formalism (400 eV energy cutoff), with a maximum of 0.03 eV/Å on each atom. The geometry optimization and frequency analysis of the target pollutant was analyzed by Gauss View 5.0.8. and Gaussian 09 via the B3LYP/6-31 G* calculations. The Fukui index was performed by Multiwfn 3.8 according to Eqs. 1–4 [43,44]:

$$f(r) = \left[\frac{\partial \rho(r)}{\partial N} \right]_{V(r)} \quad (1)$$

$$f^+(r) = q_{N+1}(r) - q_N(r) \quad (2)$$

$$f^-(r) = q_N(r) - q_{N-1}(r) \quad (3)$$

$$f^0(r) = \frac{f^+(r) + f^-(r)}{2} = \frac{q_{N+1}(r) - q_{N-1}(r)}{2} \quad (4)$$

Where $q(r)$, N, and v are respectively the electron density at a point r, the total number of electrons, and the external potential constant; f^+ , f^- , and f^0 are respectively the Fukui index in nucleophilic attack, electrophilic attack, and radical attack.

The atomic reactivity of ATZ was estimated by condensed dual descriptor (CDD) according to Eq. 5 [43,45]:

$$f^2(r) = f^+(r) - f^-(r) = 2q_N(r) - q_{N+1}(r) - q_{N-1}(r) \quad (5)$$

2.4. Catalyst synthesis

All chemicals are analytically pure and purchased from Shanghai Macklin Biochemical Co., ltd.

Synthesis of polymeric carbon nitride (PCN). The pristine polymeric carbon nitride was prepared with our previous synthetic method [7,33]. Generally, 10 g urea was milled for 10 min and placed in a covered porcelain combustion boat with a heating rate of 5 °C/min to 550 °C under static air, keeping for 4 h in a muffle furnace. After natural cooling, the bulk polymeric carbon nitride was ground into a fine powder and labeled as PCN.

Synthesis of Na-doped cyano-rich polymeric carbon nitride (NaCN). The cyano-rich Na-doped polymeric carbon nitride was prepared via the thermal condensation of urea with the existence of NaCl. The urea amount and the program setting of the muffle furnace are the same as the PCN preparation, with the addition of a certain amount of NaCl. The as-prepared powder was collected and labeled as NaCN-10, NaCN-20, NaCN-50, NaCN-100, and NaCN-200, where the additional NaCl amount was 10, 20, 50, 100, and 200 mg for each. If no specific note, the NaCN in the text and figures refer to the NaCN-100, for it exhibited the best photocatalytic performance among all these NaCN samples.

Synthesis of S, Na co-doped cyano-rich polymeric carbon nitride (NaCNS). To prepare the NaCNS, 500 mg as-synthesized NaCN-100 and a certain amount of cysteine was evenly mixed and ground. The mixed powder was then placed in covered porcelain again, heating with a 7 °C/min heating rate to 320 °C and maintaining for 2 h in a muffle furnace with static air. The naturally cooled powder was labeled as NaCNS-1, NaCNS-2, NaCNS-3, NaCNS-4, and NaCNS-5, with the cysteine addition amount of 3, 5, 10, 20, and 50 mg. If no specific note, the NaCNS in the text and figures refer to the NaCNS-3, for it exhibited the best photocatalytic performance among these NaCNS samples.

2.5. Photocatalytic performance assessment

The photocatalytic PMS activation efficiency of the catalyst was assessed by ATZ degradation. The light source was acquired via a 420 nm UV cut-off filter equipped 300 W Xe lamp. Before irradiation, 20 mg catalyst was firstly dispersed into 50 mL ATZ solution (5 ppm) and stirred (600 rpm) under dark for 20 min to ensure the adsorption-desorption equilibrium. Then, 10 mg PMS was added into the suspension for a 60-min photocatalysis. Every 20 min interval, a 2 mL suspension sample was collected and filtered with a 0.22 μm membrane, before immediately analyzing via high-performance liquid chromatography (HPLC). The residual ATZ was determined via HPLC at 225 nm with methanol and pure water (70:30 vol. ratio) as the mobile phase. To assess the reusability of the catalyst, a four-round cycling experiment has been conducted. The sampling and testing procedures are the same as the above method. After each cycle, the used catalyst was washed with ultrapure water and dried in a vacuum oven at 60 °C overnight, then collected for the next cycling test. The produced intermediates in this system were analyzed via tandem mass spectrometry (LC-MS). During the LC-MS test, 15 μL filtered samples were eluted with methanol and pure water (70:30 vol. ratio, 0.1 mL/min flow rate) via a 25 °C C18 column, before the full scan acquisition process by electrospray interface (4 kV working voltage, 400 °C).

In addition to the photocatalytic performance of the catalyst, the optical property of the photocatalysis system is also helpful for understanding the catalyst activity comprehensively [46,47]. To in-depth investigate the total rate of photon absorption per unit surface area (TRPA/A) and the optical parameter of the catalyst, the Beer-Lambert law and the six-flux model (SFM) were applied (Text S1) [48,49].

3. Results and discussion

3.1. Property of the novel photocatalysts

The NaCNS was prepared via two consecutive calcination processes (Fig. 1A). In the first calcination procedure, the urea was polymerized with the assistance of NaCl, which served as a hard template to enhance the crystallinity and endowed rich cyano groups in polymeric carbon nitride [50]. Compared to the pristine CN, a more porous structure with a smaller size of the catalyst can be observed in the SEM image of NaCN (Fig. 1B-C). The further condensation of NaCN with cysteine preserved the porous structure in the NaCNS-3 (Fig. 1D). Such rich pore structure is likely to expose more active sites for PMS activation, promote the accessibility, and boost the mass transfer between the photocatalyst and the reactant during the reaction [51,52]. Fig. 1E shows the element mapping in the NaCNS-3. Interestingly, the mapping area of sodium and nitrogen is highly consistent, indicating that the sodium dopant in NaCNS has more interaction with nitrogen than C. The structure change of the samples can be reflected via the TEM image. Consisting of the non-metallic elements, the pristine CN shows high transparency in TEM, and its HR-TEM image presents its amorphous structure (Fig. 1F and Fig. 1I). With the sodium doping, some darker dots can be observed in the TEM image of NaCN-100 and NaCNS-3, for that the metallic sodium has stronger light absorbability and present weaker transmittance (Fig. 1F-G). Simultaneously, clear lattice fringes with 3.3 Å, in accordance with the interlayer space of the heptazine units, can be observed in both NaCN-100 and NaCNS-3, indicating the enhanced crystallinity of the sample after the introduction of sodium [39].

FT-IR spectra of the pristine CN and other samples show a characteristic band of heptazine rings within the range of 1200–1600 cm⁻¹ and the stretching vibration of the aromatic C-N bond at ~810 cm⁻¹ (Fig. 2A) [7]. Comparatively, after pyrolyzing with NaCl, the NaCN samples showed a distinct cyano group peak centered at ~2160 cm⁻¹, originating from the deprotonation of the carbon-bonded amino group [30]. This peak is well-preserved in all the NaCNS samples, indicating the cyano groups can be reserved after successive thermal condensation [29]. While there are no other sulfur-related peaks shown in the NaCNS samples, which may be because the sulfur content is so small that be overlapped with other peaks [53]. XRD pattern of the as-prepared CN sample exhibited a distinct peak at 27.3° and a weaker peak at 12.7°, respectively referring to the interlayer stacking of the heptazine ring induced (002) peak and the in-plane structural packing induced (001) peak (Fig. 2B) [50]. Interestingly, the (002) peak became sharper and stronger with the sodium doping in NaCN and NaCNS samples, suggesting their more ordered structure, in accordance with the observed 3.3 Å lattice fringe in the TEM image [54]. Meanwhile, the (002) peak position of NaCN and NaCNS samples highly shifts from 27.3° to 27.6°, resulting from the shortened interlayer spacing in the photocatalyst for that the larger atomic radius of sodium and sulfur in the heptazine units that twisted the planar structure, which is beneficial to the interlayered migration of photocarriers [34,55]. The ESR spectra comparison further exhibited the increased amount of cyano groups induced nitrogen vacancies in NaCN, and NaCNS (Fig. 2C). All the ESR plots have a g value from 2.0038 to 2.0040, corresponding to the lone pair electrons in the C sp² orbital for the loss of C-N bond [29,56]. The higher g value of NaCNS (2.0040) than that of other samples (2.0038) demonstrates its promoted interaction of the electrons because the internal magnetic field can arise upon transferring electrons [57]. Obviously, the NaCN and NaCNS have a strengthened peak intensity than the pristine CN. Meanwhile, the peak intensity differences between the dark or light environment show a rising trend from CN, NaCN, to NaCNS, resulting from the promoted visible light responses and enhanced content of lone pair electrons in them. This exhibited the enhanced density state of the conduction band in NaCNS with the introduction of sodium and sulfur [58]. The cyano groups and the doped sulfur can be also found in the NaCNS via the ¹³C SSNMR spectra (Fig. 2D). Compared to the pristine CN, the NMR spectra

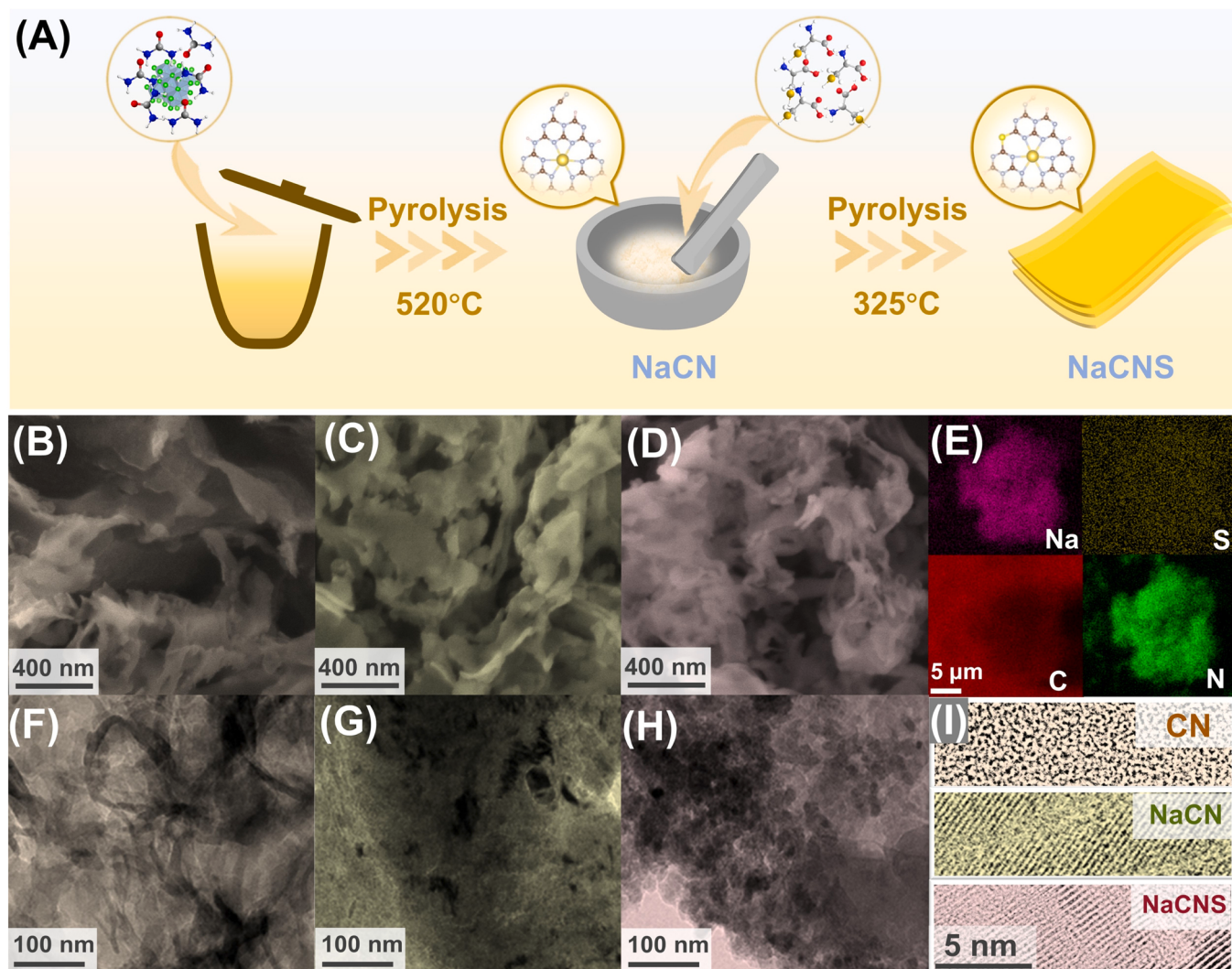


Fig. 1. (A) The schematics illustrate the synthetic process of the NaCNS; the SEM image of (B) CN, (C) NaCN-100, (D) NaCNS-3, and (E) the elemental mapping of NaCNS-3; the TEM image of (F) CN, (G) NaCN, (H) NaCNS-3, and (E) the HR-TEM image of the samples.

of NaCNS present additional cyano group peak at $\delta = 124$ ppm and a C-S peak at $\delta = 219$ ppm [59], without destroying the basic heptazine units of the CN. Given the above discussion, it can be concluded that the introduction of sodium and sulfur in the carbon nitride via the successive thermal condensation process would induce the increase of cyano groups in its heptazine-based structure. This is a crucial foundation because the preservation of the conjugated heptazine structures is the prerequisite for the delocalization of the π electrons [58].

To further determine the structural and chemical composition changes in photocatalysts, their XPS binding energy was analyzed (Fig. S1). As shown in the XPS survey spectra (Fig. S1A), all the samples have distinct C and nitrogen peaks, with a slight amount of O. The detailed elemental proportion analysis is exhibited in Fig. 2E. Apparently, with the generation of cyano group-induced nitrogen vacancy, the nitrogen proportion in NaCN is decreased. Then, the subsequent substitution of nitrogen by sulfur induced a further reduction of nitrogen proportion in NaCNS. Meanwhile, the sodium and sulfur are successively introduced into the catalyst after the pyrolysis procedure. Interestingly, the sodium content in NaCNS is slightly higher than that in NaCN, even though no additional sodium source was introduced in the second thermal condensation process. This is possible because the successive pyrolysis deepened the condensation degree and therefore increased the proportion of sodium. The detailed chemical state of the catalysts is presented in Fig. S1. Specifically, both the C-O/C≡N and

N = C-N peak (286.79 eV and 288.27 eV for each) in NaCN are positively shifted compared to pristine CN (286.60 eV and 288.22 eV for each), resulted from the electron acceptor cyano groups (Fig. S1B) [33, 60]. While with the introduction of electron donor sulfur in NaCNS, the peak position of C-O/C≡N and N = C-N are negatively shifted (286.67 eV and 288.23 eV for each). The peak position in N_{2c} of N 1 s spectra in these catalysts exhibited similar changes, demonstrating the generation of an electronic push-pull effect between the cyano groups and the sulfur doping site in the NaCNS, which is favorable for the separation of photocarriers [61,62]. The proportion of N_{2c} in each sample was calculated via their N 1 s spectra fitting (Fig. S1C). Fig. 2F summarized the C/N ratio and the N_{2c} promotion changes in the catalyst. For the successive loss of nitrogen during the generation of nitrogen and the substitution of nitrogen by sulfur, the C/N ratio in CN, NaCN, and NaCNS showed an increasing trend. Meanwhile, the ratio of N_{2c} to the total nitrogen showed a decrease in tendency from CN to NaCN and NaCNS. The initial decreases can be attributed to the generation of cyano groups at the original N_{2c} site during the NaCl etching process. Then the drop of N_{2c} from NaCN to NaCNS is possible because of the substitution of N_{2c} sites by the doping sulfur [63]. Besides, a new O 1 s peak at 535.40–535.70 eV is shown in NaCN and NaCNS (Fig. S1D), assigned to the adsorbed oxygen species on the nitrogen vacancy site [29]. Such adoption of oxygen species in the catalyst is essential for the photocatalytic procedure because the imitated contact can effectively

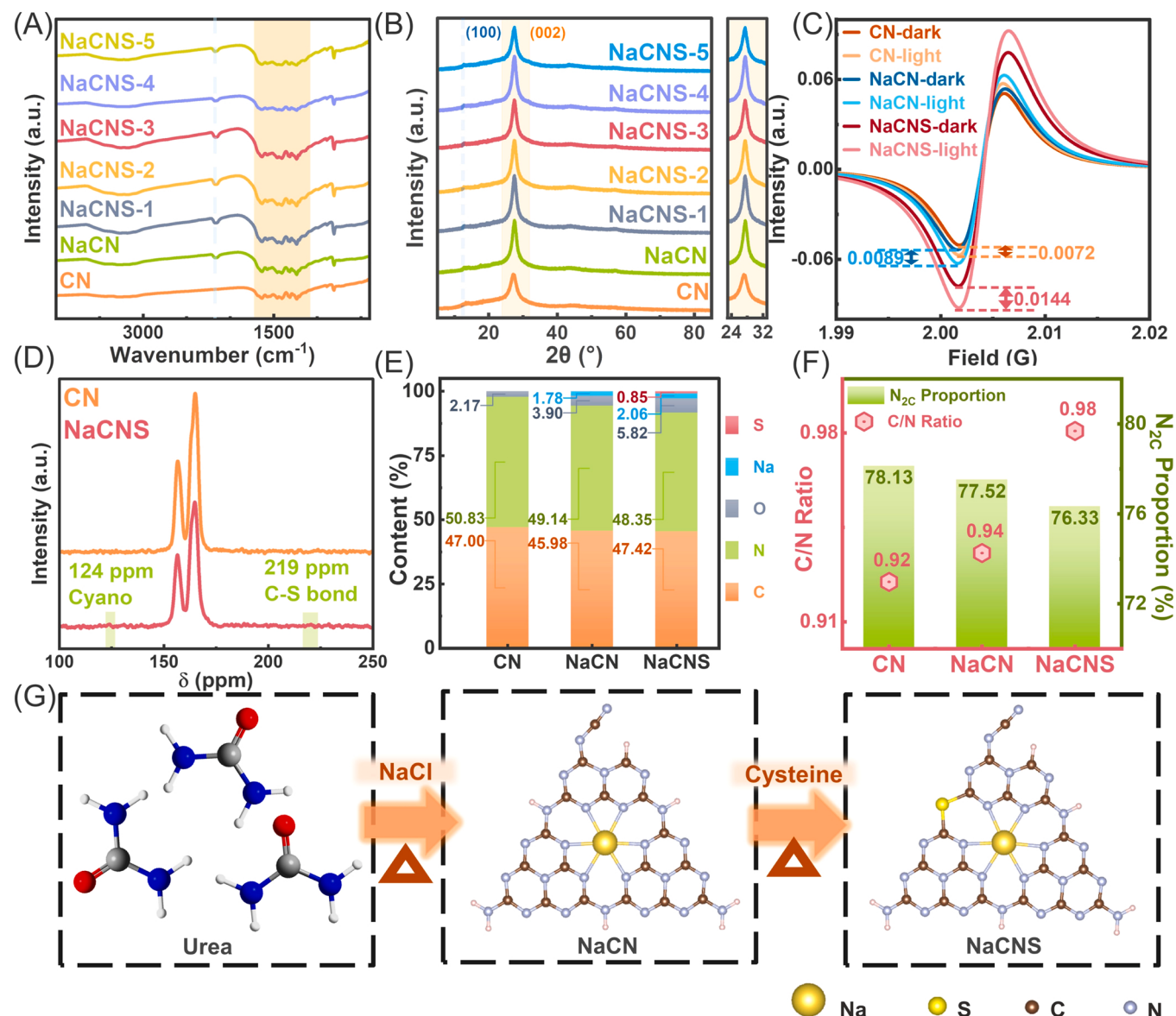


Fig. 2. The structural analysis of the NaCNS sample. (A) The FT-IR spectra, (B) the XRD spectra, the (C) ESR spectra and (D) ^{13}C SSNMR spectra, and the (E-F) chemical composition comparison between the samples; (G) schematics illustrate the structural change of the samples during the pyrolysis process.

accelerate the generation of ROS. The Na 1 s spectra of the NaCN and NaCNS show peaks at a similar position (~ 1071.8 eV) for the existence of the Na-N interaction, implying that the alkali Na is coordinated with the bridging N of the heptazine units [55,64,65]. This is highly consistent with the elemental mapping result (Fig. 1E). Given the above analysis, along with the XPS S 2p spectra of the catalysts, it can be convinced that the sodium and sulfur have been successively doped into the CN backbones. Also, the above information provides a reliable basis for the subsequent modeling. As Fig. 2G shows, the pyrolysis of urea with the existence of NaCl would induce the etching of the heptazine unit and produce the nitrogen vacancy with cyano group forms. Meanwhile, the alkali Na was preserved in the heptazine framework and interacted with the bridged nitrogen. In NaCNS, the further thermal condensation of cysteine and NaCN induced the substitution of the N_2C . To find the rational site of the doping sulfur, 9 models with different S sites have been built (Fig. S2). When the sulfur is doping at the S9 site, the total energy of NaCN is the lowest, suggesting that S9 is the more likely sulfur-doped site. Therefore, the subsequent theoretical calculation was performed by the S9 model (Fig. 2G).

With the consecutive modification of the carbon nitride-based

composites, the CN, NaCN, and NaCNS samples show an increasingly darker color (Fig. S3). The introduction of cyano groups and the heteroatoms are likely to change the light responses of the catalysts, which can directly affect their color. Therefore, the UV-vis-NIR DRS spectra of different samples were evaluated to acquire more detailed information (Fig. 3 A). As the pristine CN, all the samples preserved the $\pi-\pi^*$ electron transitions of the sp^2 hybridization in the heptazine unit framework (at ~ 390 nm wavelength), with a certain level of redshift [66,67]. Comparatively, NaCN has a stronger light absorption intensity than CN, and the NaCNS samples show further strengthened light absorption, within the wavelength range of 500–800 nm. Specifically, the NaCN and NaCNS samples showed a promoted light absorption within the range from 450 to 800 nm, and such a trend was deepened with the increasing amount of sulfur. Such change is likely originating from the cyano groups and sulfur doping, for this change may arise more lone pairs of nitrogen atoms and deform the planar heptazine structure, leading to an easier excitation of n electrons to the antibonding π^* orbitals [33,67,68]. Combining the tauc plots and the XPS VB spectra of the catalysts (Fig. 3B-C), the electronic band configuration can be estimated (Fig. 3D). With the successive modification of the CN, NaCN,

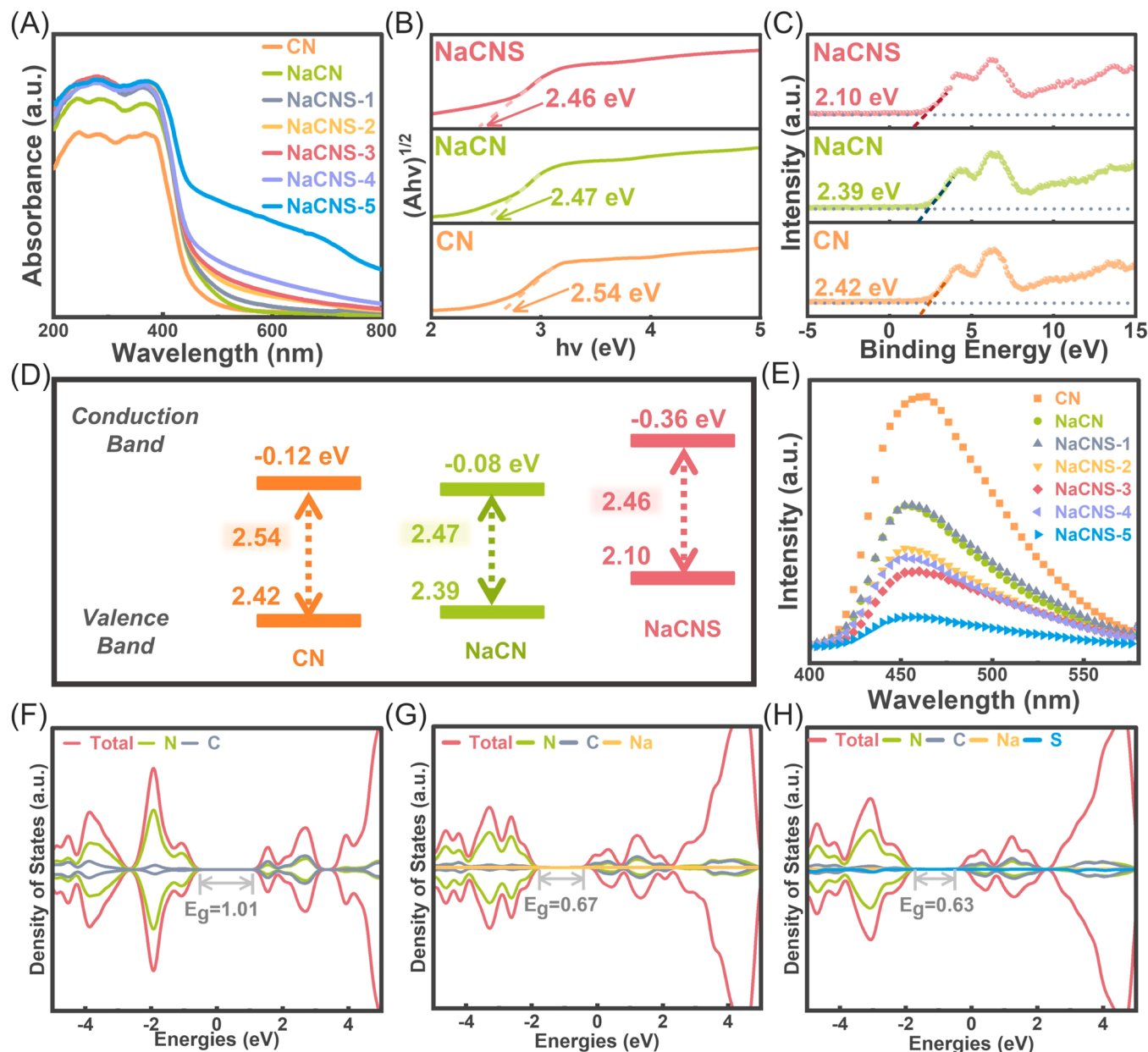


Fig. 3. (A) The UV–vis–NIR DRS spectra, (B) corresponding tauc plots, (C) XPS valence spectra and the electronic band configuration, and the (E) photoluminescence emission spectra of the samples; (F) the density of state in different catalysts calculated by DFT calculation.

and NaCNS, their valence band maximum (VBM) position was slightly decreased from 2.42, 2.39, to 2.10 eV. The bandgap of CN, NaCN, and NaCNS was calculated to be 2.55, 2.47, and 2.46 eV for each. Therefore, the conduction band (CB) of CN, NaCN, and NaCNS can be respectively estimated to be -0.12 , -0.08 , and -0.36 eV via $E_g = E_{VB} - E_{CB}$ [69,70]. It can be noted that the involvement of sodium and the production of cyano groups mainly changed the band gap, and the replacement of nitrogen by sulfur is mainly responsible for the upward shift of VBM. Finally, with the above-mentioned efforts and the construction of an electron push-pull system, the migration and separation of excitons can be dramatically accelerated [71]. Though the decrease in bandgap energy can boost the excitation of photoelectrons, it may also possibly hinder the dissociation of excitons. The PL spectra were also assessed to evaluate the recombination of the photocarriers in different samples. The strongest curve intensity of pure CN indicates its relatively higher recombination rate in photogenerated electrons and holes (Fig. 3E). That in NaCN was apparently lowered because the introduced sodium

chlorine during the reaction can effectively enhance the crystalline to promote the effective charge transfer [26], also the produced cyano groups can act as an electron acceptor to facilitate the directional movement of photocarriers [29]. The further doping of sulfur in the NaCNS gives a further flattened PL curve. The more sulfur content, the lower the photoluminescence emission signal, indicating the better exciton association in the samples. To in-depth understand the electronic configuration change along the consecutive modification, the DFT calculation on band structure and total density of state (TDOS) in the samples was performed (Fig. 3F–H and Figs. S4A–C). Apparently, the two-step modification could affect the band structure of the sample to a different extent. Especially, the bandgap changes in the TDOS spectra show the exactly same trend as the calculated from tauc plots: the band gap of NaCN (0.67 eV) is dramatically shortened than that in CN (1.01 eV) for the introduction of cyano groups, while further doping of sulfur in NaCNS (0.63 eV) would not show a significant change. This further demonstrated that sodium chloride mainly plays a role in

narrowing the bandgap [34]. According to the enlarged partial density of states (PDOS), it was found that the VBM of all the samples is mainly attributed to the C 2p electrons and the VBM of them mainly depends on the N 2p electrons. The visualized deformation charge density comparison between CN and NaCNS can better illustrate the charge distribution change after modification (Figs. S4D-E). The introduction of cyano and sulfur in NaCNS can break the symmetric heptazine structure, leading to a less uniform distribution of electrons or holes, and facilitating the separation of the charge carriers [29]. Interestingly, a larger electron depletion area is shown around the cyano-groups induced nitrogen-vacancy and a new electron accumulation area is formed at the sulfur doping site, originating from the electronic push-pull effect in the catalyst for better separation of electrons and holes. Besides, the surface charge distribution of NaCNS shows the apparent charge transfer between the doped sodium atom and the carbon nitride substrates (Fig. S4F), originating from the strong interaction between them. In this case, the sodium in NaCNS can act as an electronic migration channel to

strengthen the charge transfer, not only within the heptazine framework, but also between the PMS and the catalyst [72]. Similarly, the structural change in photocatalysis can also induce the difference in the electronic distribution of their CBM or VBM (Fig. S5). The CBM and VBM in the pristine CN are highly consistent, which is likely to induce a high combination rate of the electrons and holes. In NaCN, VBM tends to be centered around the cyano group, meanwhile, the overlap area of electrons accumulation and electron depletion has largely reduced, no matter whether in VBM or CBM, indicating the construction of NaCN can effectively rearrange the electronic band configuration for promoting the charge transfer [33]. The introduction of sulfur in NaCNS can further enhance the electron accumulation or depletion area in both VBM and CBM, indicating more excitable electrons in the sample [30].

3.2. Photocatalytic performance evaluation

Before evaluating the PMS activation ability of the catalysts, the

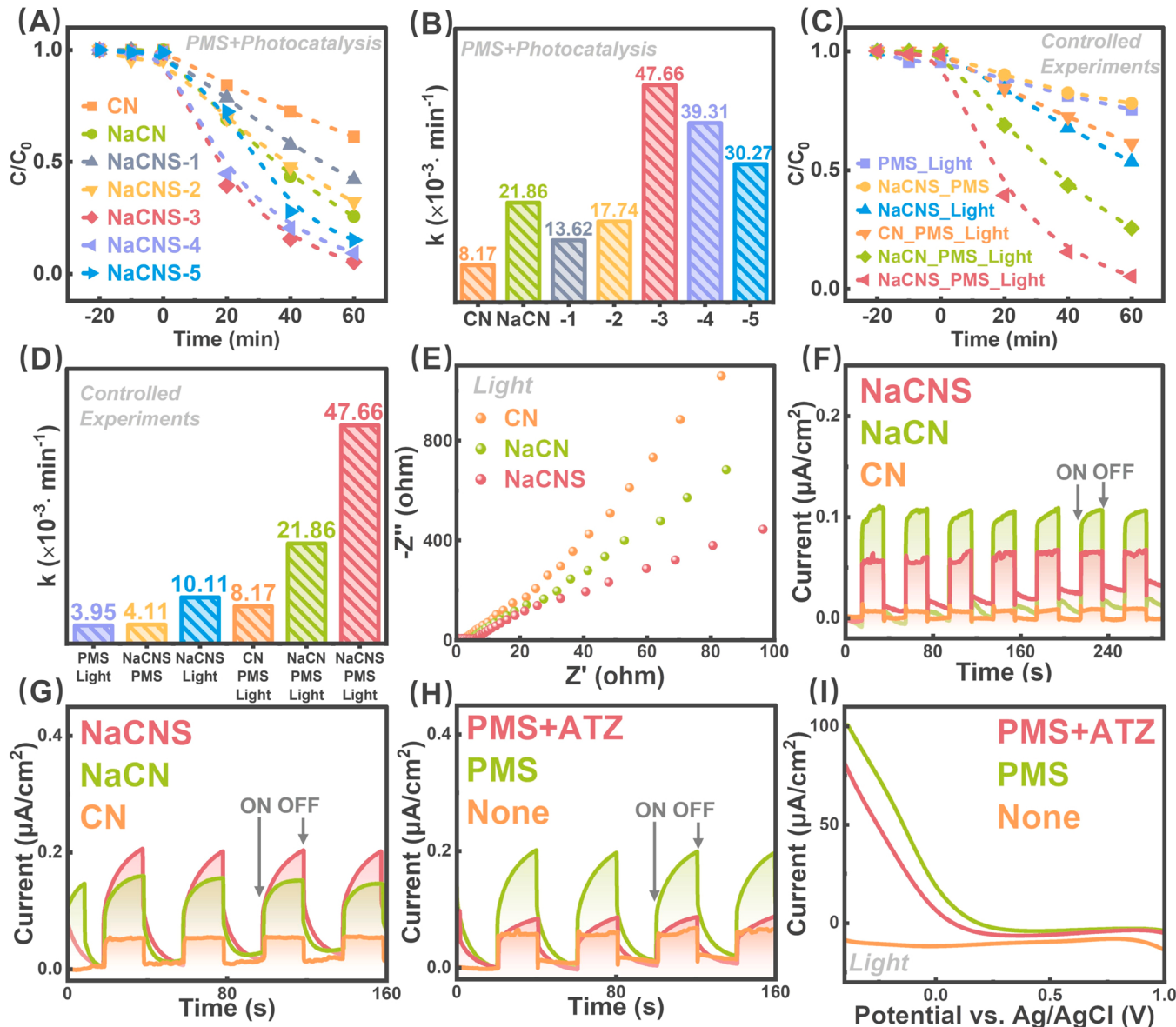


Fig. 4. (A) The photocatalytic PMS activation efficiency for ATZ degradation by a different catalyst, (B) and the accordance reaction rate constant; the controlled experiments for the photocatalytic PMS activation efficiency of the NaCNS sample, and (D) the accordance reaction rate constant; (E) EIS plots of CN, NaCN, and NaCNS under visible light; the photocurrent of the different sample (F) without or (G) with the existence PMS; (H) the photocurrent comparison and the (I) LSV curves of NaCNS with a different solution.

fabrication of NaCNS was optimized via serials photocatalytic ATZ degradation assessment. Firstly, the optimal sodium chloride addition dose for NaCN samples was evaluated (Figs. S6A–B). The introduction of cyano groups and sodium ions by sodium chloride can respectively form an electron acceptor and construct an electronic migration channel to facilitate the separation of photocarriers and the mass transfer in the system [34]. Therefore, the majority of the NaCN samples, except NaCN-200, showed enhanced photocatalytic efficiency than the pristine CN, achieving a 25–35% ATZ removal rate. The photocatalytic ATZ degradation by NaCNS-200 (10% removal rate) was weaker than pure CN (25% removal rate), which can be attributed to the excessive sodium chlorine added during the fabrication process breaking up the heptazine-based structure of carbon nitride, leading to the loss of photocatalytic activity [29]. Especially, the NaCN-100 showed the best performance for ATZ degradation, reaching 35% ATZ removal, and thus applied in the subsequent modification. The sulfur doping in the NaCN sample can further change the ATZ degradation behavior for the electronic band adjustment effect by sulfur (Figs. S6C–D). Thereinto, NaCNS-2, 3, 4 with appropriate sulfur doping amount shows enhanced photocatalytic ATZ degradation efficiency (37–58% removal rate). Then, the photocatalytic PMS activation ability of these catalysts was further evaluated via the ATZ degradation (Fig. 4 A). It was found that all the samples demonstrated a certain PMS activation effect, and the ATZ degradation in these systems follow pseudo-first-order kinetics (Fig. S6F). With the assistance of PMS, the ATZ degradation by CN raised to 39%, and the reaction rate constant (k) was calculated as $8.17 \times 10^{-3} \cdot \text{min}^{-1}$ (Fig. 4B). The NaCN has a more distinct photocatalytic PMS activation effect, which can degrade 74% ATZ within 60 min, and the accordance k value is more than twice as big as CN, enhanced to $21.86 \times 10^{-3} \cdot \text{min}^{-1}$. With the further addition of sulfur, the NaCNS-1 and NaCNS-2 with a small quantity of sulfur show a slightly weaker ATZ degradation than NaCN, only 58% and 68% for each. This can be attributed to that the too-small amount of sulfur in the sample may not be enough to effectively regulate the band structure. The ATZ degradation by NaCNS-3, NaCNS-4, and NaCNS-5 in the photocatalytic PMS activation system has a promoted effect than both CN and NaCN. Comparatively, the NaCNS-3 shows the most effective ATZ degradation, achieving a 95% removal rate with $k = 47.66 \times 10^{-3} \cdot \text{min}^{-1}$, which was 5.83 times more than the pristine CN. The slightly weaker effect of NaCNS-4 and NaCNS-5 than NaCNS-3 is possibly attributed to the excessive sulfur doping in the photocatalyst that breaks the photocatalytic active unit and induced the deactivation of the catalyst [73]. By comparing the photocatalytic ATZ degradation in the controlled experiments, a more interesting phenomenon can be observed (Fig. 4 C). Without any catalysts, the ATZ degradation rate by the photocatalytic PMS activation within 60 min can reach 24% with $k = 3.95 \times 10^{-3} \cdot \text{min}^{-1}$. The introduction of photocatalysts during the photocatalytic PMS activation can effectively promote the decomposition of ATZ (Fig. S6F and Fig. 4D). Specifically, without visible light, the NaCNS can activate PMS to degrade 22% ATZ within 60 min $k = 4.11 \times 10^{-3} \cdot \text{min}^{-1}$. While without the PMS, the NaCNS can photocatalytically degrade 47% ATZ, $k = 10.11 \times 10^{-3} \cdot \text{min}^{-1}$. Either the sum of the ATZ removal rate or the reaction rate constants in the NaCNS/light and NaCNS/PMS system is less than those in NaCNS/PMS/light system, indicating that the NaCNS can trigger the synergistic effect of light and PMS during the ATZ degradation [19,74]. With the synergistic effect, the ATZ degradation efficiency in this system is more effective than in many previous studies (Fig. S6G) [12,19,75–79].

To further understand the optical property differences between the catalyst, the absorption of catalyst suspension was evaluated to estimate the optical coefficients of different catalysts (Table S1). Interestingly, though the absorption of CN and NaCN powder samples was obviously weaker than the NaCNS samples, their suspension showed a stronger absorption (Fig. S7A). Such variations in suspension absorbance are possibly arising from the morphology differences between the catalysts, which is consistent with similar studies [29]. Similarly, the extinction

coefficient, scattering coefficient, absorption coefficient optical thickness (τ), apparent optical thickness (τ_{app}), and the TRPA/A of CN and NaCN suspension samples are distinctly higher than the NaCNS suspension samples. This indicated that the optical parameter of the catalyst has limited impact on the photocatalytic system in this work, for the photodegradation of contaminants not only depended on the light absorption of the catalyst but also depended on the mass transfer. The better photocatalytic ATZ degradation in the NaCNS-dominated PMS activation system is likely resulting from the dual modification of NaCNS that accelerate the PMS activation and the mass transfer in the system. Specifically, the higher TRPA/A value of the NaCNS-3 sample exhibited its better photon absorption ability than other NaCNS samples. It is worth mentioning that the optimized τ_{app} generally located within 1.8–4.4. Therefore, excepting the pristine CN, the photocatalytic performance of other samples was compared within the optimal τ_{app} range. The photon absorption of the catalyst is closely related to their τ_{app} and would directly affect the ATZ degradation, a further comparison of all the catalysts thus carried out at an equal τ_{app} (3.47) as NaCNS-3. Therefore, the experimental catalyst dosages of CN, NaCN, NaCNS-1, NaCNS-2, NaCNS-4, and NaCNS-5 were respectively calculated to be 1.04, 0.46, 0.33, 0.35, 0.32, and 0.32 g/L (Fig. S7B). At the equal τ_{app} value, the CN and NaCN exhibited stronger photocatalytic performance than in the controlled experiment, while still showing weaker ATZ removal than NaCNS-3, 4, 5. Thereinto, the NaCNS-3 sample still shows the best ATZ degradation, double confirming the effectiveness of dual modulation on the catalyst in this photocatalytic PMS activation system.

To further compare the electrochemical property differences in the catalyst and the photoelectric response changes in different systems, an electrochemical workstation was applied to conduct serials of controlled experiments. Electronic impedance spectroscopy (EIS) curves reveal the charge transfer ability and the electrode ion diffusion process of the catalysts (Fig. 4E). Under visible light, the largest slope of the CN curve indicates its relatively higher electrochemical impedance [80]. With the electron acceptor effect of cyano groups and the sodium electronic migration channel, the electronic separation and migration were effectively promoted, and the electrochemical impedance in NaCN was shortened. Further introduction of sulfur in NaCNS imports an electron donor element, leading to the electronic push-pull effect and further adjusting the electronic band configuration in NaCNS. Therefore, the electronic migration in the system can be further accelerated [53,63]. In the dark environment, this electrochemical impedance change trend is also obeyed with slightly larger slopes, indicating that visible light can promote charge transfer in the catalysts. Fig. 4 F shows the photocurrent response comparison of the samples. The pristine CN shows the weakest photocurrent responses, with only $0.01 \mu\text{A}/\text{cm}^2$. In NaCN and NaCNS samples, the photocurrent density under light was respectively raised to 0.10 and $0.07 \mu\text{A}/\text{cm}^2$. The photocurrent density of NaCN was higher than NaCNS and seems not to conform to the ATZ degradation trend of them. Considering the complex process involved during ATZ degradation, including the generation of photocarriers and the mass transfer in the system, the NaCNS may also accelerate ATZ degradation by boosting the mass transfer process during the reaction [81]. The photocurrent response of the catalysts in the PMS solution was further evaluated to investigate the photocarrier migration in the electrodes (Fig. 4 G). With the addition of PMS, the photocurrent of all these samples was significantly enhanced, indicating all these catalysts can react with PMS for reactive species during photocatalysis [82]. Compared to NaCN ($0.15 \mu\text{A}/\text{cm}^2$) and CN ($0.05 \mu\text{A}/\text{cm}^2$), the NaCNS shows the best PMS activation efficiency, where the photocurrent response increased to $0.21 \mu\text{A}/\text{cm}^2$ from $0.07 \mu\text{A}/\text{cm}^2$. Upon the addition of ATZ in the solution with PMS, the photocurrent on NaCNS exhibited an obvious negative change, suggesting the electron transfer from ATZ to PMS via the NaCNS catalyst (Fig. 4H) [26,82,83]. Similarly, the linear sweep voltammetry (LSV) curves showed the same tendency (Fig. 4I). Much higher current was observed in the solution with PMS than the electrolyte, suggesting

that the assistance of PMS can reduce the energy consumption and enhance the ATZ degradation. The slightly lowered curve after ATZ addition demonstrated the charge migration in the systems.

The ATZ degradation efficiency in this system is related to the experimental parameters, the impact of various catalyst dosages and PMS dosages was thus assessed. The adsorption of ATZ by the catalyst was negligible with various dosages, and the ATZ degradation rate is positively related to the catalyst dosage (Fig. 5A and Fig. S9A). When the catalyst dosage decreased from 0.4 to 0.1 g/L, the ATZ removal rate only slightly dropped from 95% to 92%, and k values ranged from 47.66 to $44.90 \times 10^{-3} \cdot \text{min}^{-1}$. When the catalyst dosage further decreased to 0.05 g/L catalyst, 74% ATZ can be removed, indicating the effective catalytic efficiency of NaCNS in this photocatalytic PMS activation system. Comparatively, the PMS dosage was also positively related to ATZ degradation, with a more obvious change in k value (Fig. 5B and Fig. S9B). When the PMS dosage was 0.05 g/L, the k value for ATZ degradation was $16.52 \times 10^{-3} \cdot \text{min}^{-1}$. When the PMS dosage increased to six times (0.3 g/L), the k value increases nearly eightfold ($127.44 \times 10^{-3} \cdot \text{min}^{-1}$). This indicates that the NaCNS can effectively activate high-dose PMS, converting them into reactive species, and achieving highly efficient ATZ degradation. The pH value also plays a key role in the water treatment, the ATZ solution was therefore regulated to a wide pH range from a strong acidic to a strong alkali environment (Fig. 5C and Fig. S9C). The ATZ degradation potency is obviously better under acidic conditions, and k even reaches $100.72 \times 10^{-3} \cdot \text{min}^{-1}$ when pH= 3. When pH rises from 3 to 9, the ATZ degradation rate within 1 h could maintain a steady level, above 93%. However, a strong base condition (pH=11) is not conducive to ATZ degradation, where the ATZ removal rate dramatically dropped to 53%, with $k = 12.09 \times 10^{-3} \cdot \text{min}^{-1}$. Under a base condition, the $\cdot\text{SO}_4^-$ is likely to react with OH^- and generate $\cdot\text{OH}$. The lower oxidation potential and shorter lifetime of $\cdot\text{OH}$ than $\cdot\text{SO}_4^-$ was therefore impaired the ATZ degradation in this system [84,85]. Such a phenomenon can be also

observed in the co-existing ions experiment (Fig. 5D and Fig. S9D). With the presence of alkaline anions, such as HCO_3^- and CO_3^{2-} , the ATZ degradation rate was only 59% and 46% for each, with $k = 16.33$ and $11.14 \times 10^{-3} \cdot \text{min}^{-1}$. The existence of SO_4^{2-} shows a slightly promoting effect on ATZ degradation, and the existence of NO_3^- and Cl^- was much more significant. Interestingly, the ATZ degradation efficiency with these co-existing ions is highly related to their acidity. The more acidic the coexisting ion is, the larger the k value is. This further confirmed the effect of pH on the ATZ degradation in this system. In addition, the co-existing Cl^- can trigger an extremely high k value ($200.37 \times 10^{-3} \cdot \text{min}^{-1}$) for ATZ degradation, for the Cl^- can directly react with $\cdot\text{SO}_4^-$ and OH^- and transformed into Cl , $\cdot\text{Cl}_2$, and $\cdot\text{HClO}^-$, facilitating the ATZ degradation [86,87]. The influence of natural organic matter (NOM) on the ATZ degradation in this system was also assessed (Fig. 5E and Fig. S9E). When 10 mg/mL fulvic acid (FA) and humic acid (HA) were added to the solution, the ATZ degradation rate apparently decreased to 69% and 61% for each. The HA and FA generally contain phenolic hydroxyl and carboxyl groups, which could interact with the active site of the catalyst, adsorbed on it and inhibit the mass transfer between the catalyst, PMS, and ATZ, and induced blocked ATZ degradation [88]. While the addition of CA dramatically enhanced the efficiency of this system, because the CA can not only induce an acidic environment but also can transform into $\cdot\text{OH}$ to strengthen the ATZ removal in this system [89]. With only 20 min, the ATZ could be completely degraded with $k = 210.13 \times 10^{-3} \cdot \text{min}^{-1}$. To further estimate the potential practicality of this system, actual water was acquired to prepare the ATZ solution (Fig. 5F and Fig. S9F). The tap water generally contains residual chlorine, which is possibly converted into reactive species to promote ATZ degradation [90]. The ATZ degradation rate in filtered tap water reached 99% after 1 h. Comparatively, river water has a much more complex composition, including soluble natural organic matter, various ions, and other impurities. Therefore, the ATZ degradation in river water was slightly inhibited to an 87% removal rate

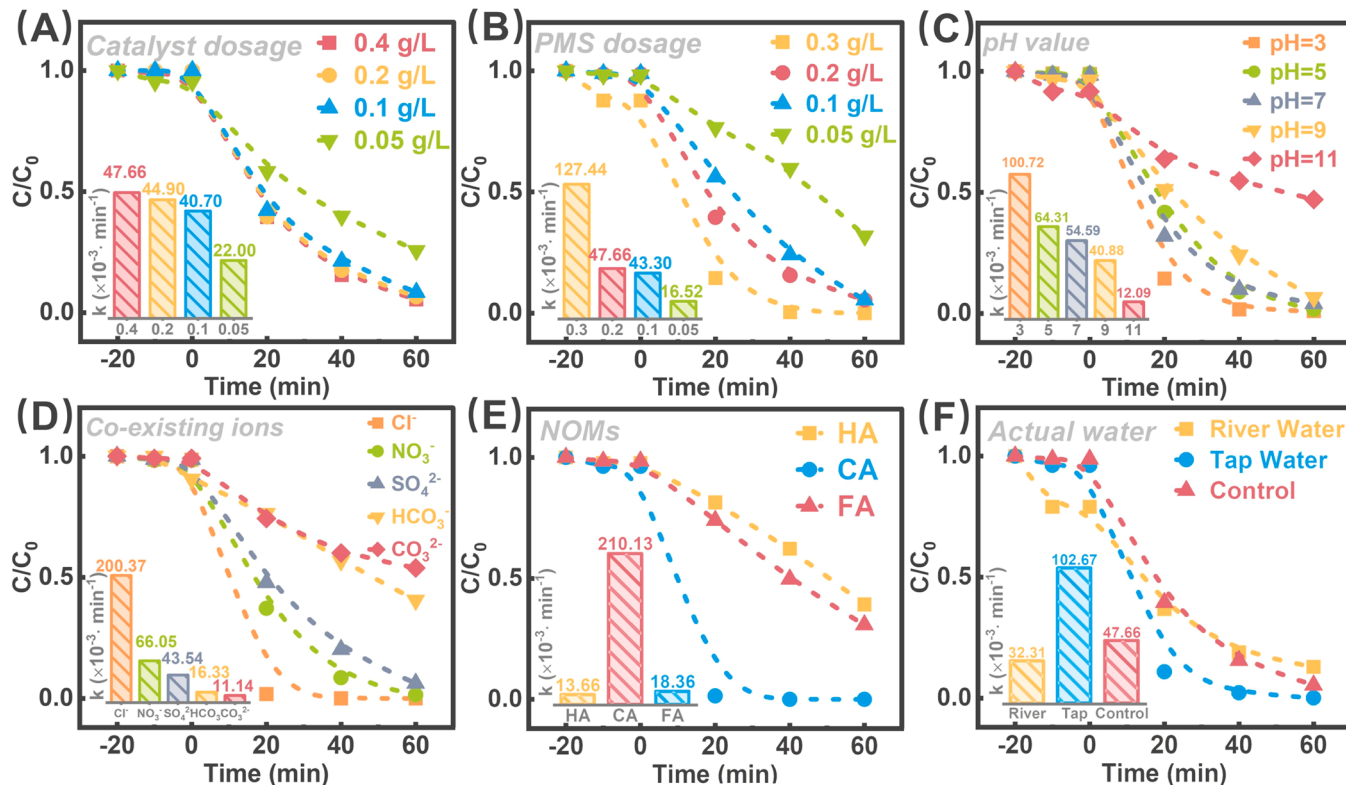


Fig. 5. The photocatalytic PMS activation efficiency for ATZ degradation with various (A) catalyst dosage, (B) PMS dosage, (C) pH value, (D) co-existing ions, (E) NOMs, and (F) actual water.

[91]. Moreover, a 4-cycle recycling test of the catalyst has been conducted and demonstrated the potential practicality of the system (Fig. S9G). After four rounds, the ATZ removal rate in this photocatalytic PMS activation system is basically stable, slightly decreasing from 95% to 83%.

3.3. Photocatalytic mechanism

3.3.1. Potential photocatalytic mechanism

In order to understand the PMS activation efficiency differences between CN and NaCNS, the PMS adsorption and activation process on them was investigated via transition state calculation (Fig. 6). Before adsorption, the O-O bond length of the free PMS was calculated to be 1.416 Å (Fig. S10). When PMS was adsorbed on CN and NaCNS samples, referring to their initial state (IS), the O-O bond length in PMS was respectively prolonged to 1.473 and 2.506 Å (Figs. S11-12). The much longer O-O bond in NaCNS-adsorbed PMS than CN-adsorbed PMS illustrates its easier PMS activation capacity [25,92]. Interestingly, it was found that the sulfate prefers to interact with CN at the catalyst edge, while in the case of NaCNS, the sulfate is more likely to interact with the centered sodium atoms, no matter in the transition state (TS) or final state (FS). Besides, the Na in NaCNS is significantly elevated from the heptazine unit for such a strong interaction effect. Such interaction between sodium and PMS can facilitate anchoring and activating PMS for better mass transfer between PMS and catalyst, generating more reactive species [50]. Meanwhile, the sodium offers a robust structural base site, exhibiting a strong sulfation-resistant ability to extend the working life of the catalyst [37,39]. The energy barrier of PMS transition on CN or NaCNS was also determined. The negative adsorption energy of PMS on

NaCNS and CN indicates they both are thermodynamic spontaneous processes, while the more negative value in NaCNS (-2.73 eV) than CN (-0.96 eV) indicates that the modification of CN can effectively accelerate this process. Similarly, NaCNS showed a better performance in stabilizing the PMS TS, resulting in a decreased energy barrier than CN (3.40 eV vs. 5.69 eV). The easier PMS adsorption and activation on NaCNS further demonstrated the non-negligible role of sodium and cyano groups in PMS activation.

The produced reactive species by PMS activation in this system were determined via quenching experiment and the ESR trapping of the species. During the photocatalytic PMS activation process, $\cdot\text{SO}_4^-$, h^+ , $\cdot\text{O}_2^-$, $^1\text{O}_2$, and $\cdot\text{OH}$ all may affect the degradation of the contaminants, their sacrificial agent including MeOH (100 mM, $\cdot\text{SO}_4^-$ and $\cdot\text{OH}$ quencher), EDTA-2Na (2 mM, h^+ quencher), BuOH (2 mM, $\cdot\text{OH}$ quencher), p-BQ (2 mM, $\cdot\text{O}_2^-$ quencher), and FFA (2 mM, $^1\text{O}_2$ quencher) was therefore respectively added into the ATZ solution to access their contribution (Fig. 7A-B) [7,33]. When MeOH, EDTA-2Na, and BuOH were added to the solution, the ATZ removal rate was maintained above 92%. Thereinto, the lower k value in MeOH ($34.71 \times 10^{-3} \cdot\text{min}^{-1}$) than BuOH ($46.22 \times 10^{-3} \cdot\text{min}^{-1}$) involved ATZ degradation accounts for the higher contribution of $\cdot\text{SO}_4^-$ than $\cdot\text{OH}$. Meanwhile, the negligible effect of EDTA-2Na ($k = 44.23 \times 10^{-3} \cdot\text{min}^{-1}$) implied that the ATZ degradation in this photocatalytic PMS activation system was dominated by the photogenerated electrons rather than holes. Comparatively, $^1\text{O}_2$ and $\cdot\text{O}_2^-$ exhibited a considerable effect on the ATZ degradation in this system, which can respectively weaken ATZ removal rate to 10% and 19%, and the k for each reaction was only $1.58 \times 10^{-3} \cdot\text{min}^{-1}$ and $4.14 \times 10^{-3} \cdot\text{min}^{-1}$ for each. The relative contribution of each reactive species to the ATZ degradation was estimated via Eqs. 6–10. The relative

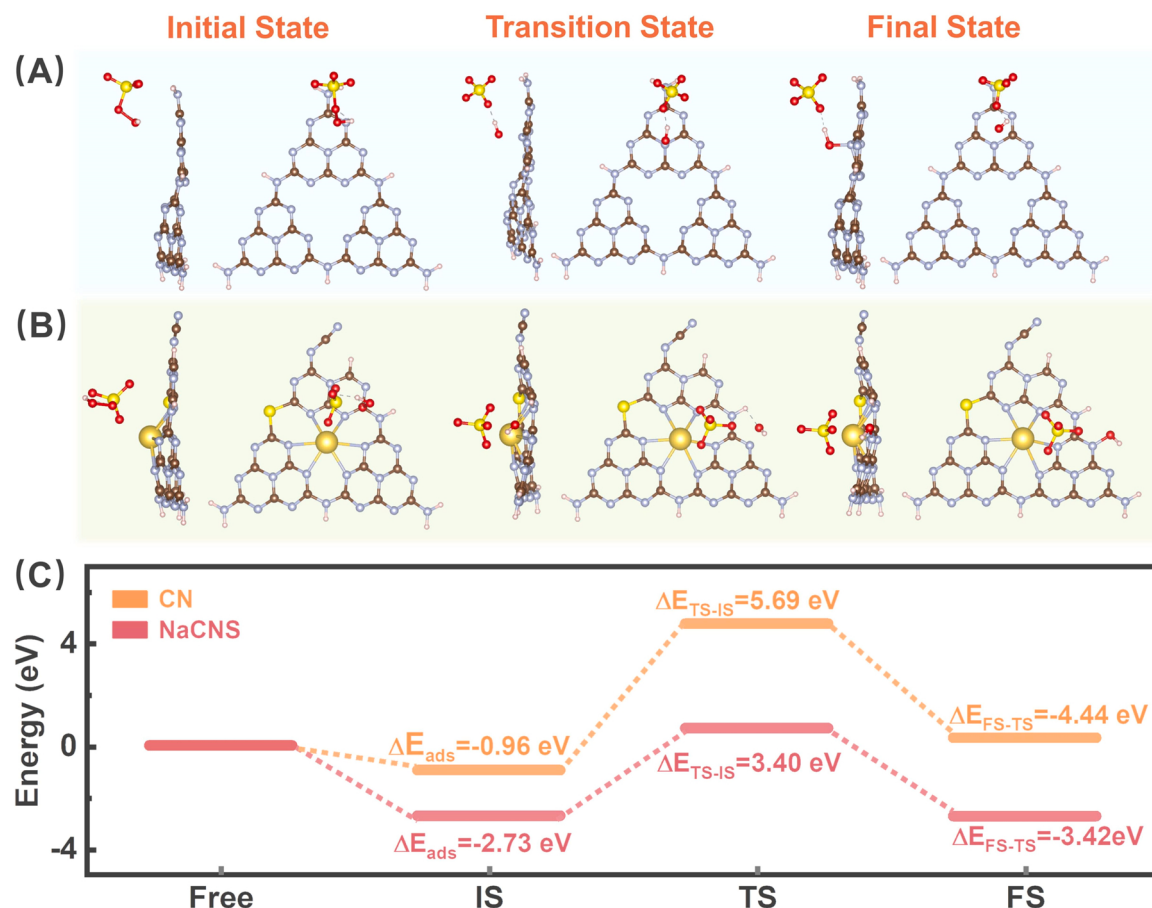


Fig. 6. The PMS activation path simulation. The top view (left) and side view (right) of the optimized structures show the interaction between PMS and (A) CN or (B) NaCNS at different PMS activation states; (C) the energy change of the PMS activation process on CN or NaCNS.

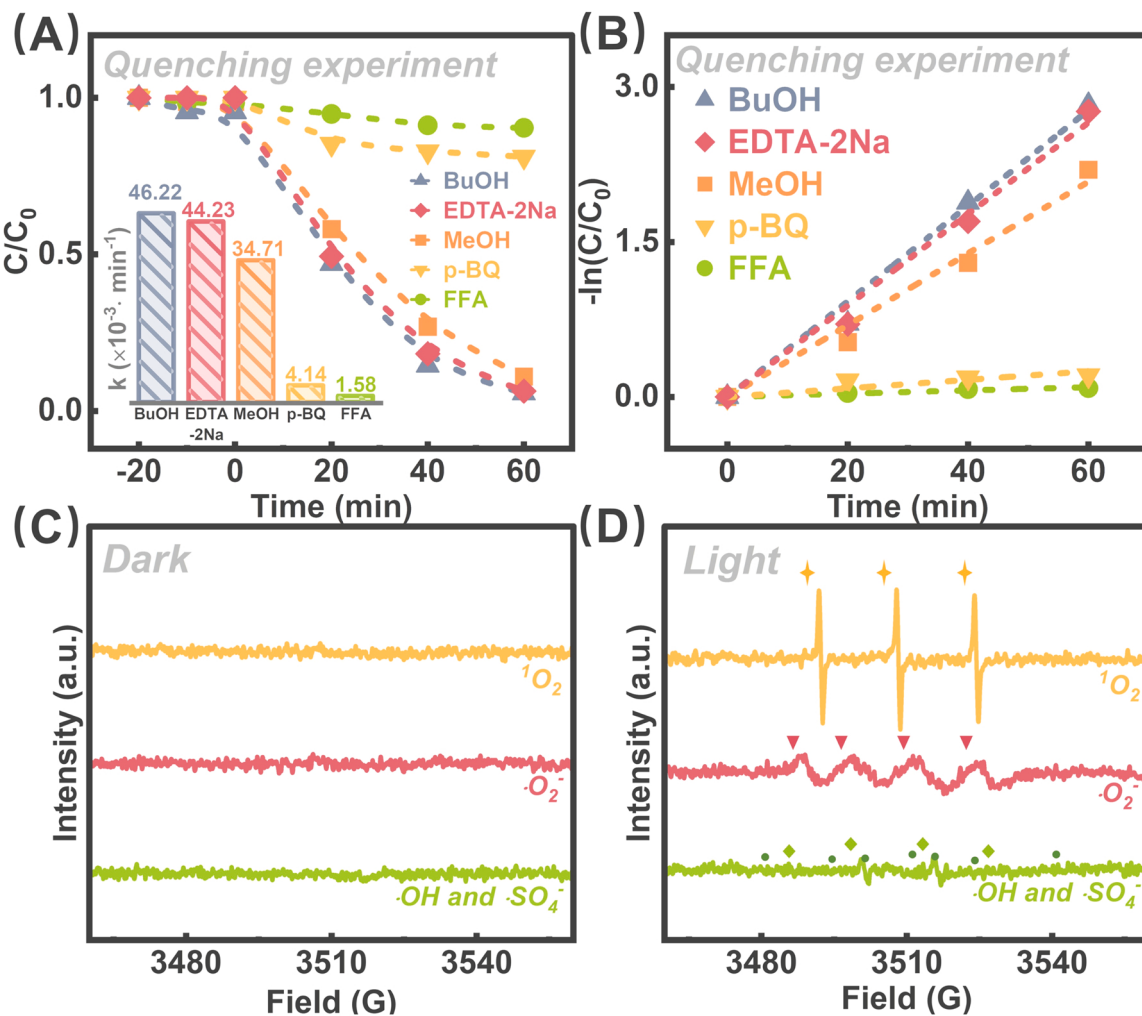


Fig. 7. The determination of reactive species in the photocatalytic PMS activation system. (A) The ATZ degradation curve with various sacrificial agents and (B) the corresponding pseudo-first-order kinetics; The ESR signal of the reactive species in (C) dark or (D) light environment.

contribution of $\cdot\text{OH}$, $\cdot\text{SO}_4^-$, h^+ , $\cdot\text{O}_2^-$, and $^1\text{O}_2$ were respectively calculated to be 3%, 24%, 8%, 91%, and 97%. It is worth mentioning that the proportion sum of each contribution is greater than 100%, for the interconversion of active species, especially the $\cdot\text{O}_2^-$ and $^1\text{O}_2$ [14]. The very close contribution rate between $\cdot\text{O}_2^-$ and $^1\text{O}_2$ also indicate that the $\cdot\text{O}_2^-$ mainly act as an intermediate to produce $^1\text{O}_2$ [93]. The reactive species contribution result indicates that the ATZ degradation in this photocatalytic PMS activation system is dominated by $^1\text{O}_2$ involved non-radical pathways [26]. The generation of the above reactive species was also verified by ESR detection. Under a dark environment, no species can be detected, even with the existence of PMS. While with visible light irradiation, the $\cdot\text{OH}$, $\cdot\text{SO}_4^-$, $\cdot\text{O}_2^-$, and $^1\text{O}_2$ can be clearly shown. Specifically, the signal intensity of $^1\text{O}_2$ is the highest while $\cdot\text{OH}$ and $\cdot\text{SO}_4^-$ is much weaker, which is very similar to their relative contribution rate.

$$R_{\cdot\text{OH}} = \frac{k_{\cdot\text{OH}}}{k_{app}} \approx 100\% - \frac{k_{\text{BuOH}}}{k_{app}} \quad (6)$$

$$R_{\cdot\text{SO}_4^-} = \frac{k_{\cdot\text{SO}_4^-}}{k_{app}} \approx \frac{k_{\text{BuOH}} - k_{\text{MeOH}}}{k_{app}} \quad (7)$$

$$R_{\text{h}^+} = \frac{k_{\text{h}^+}}{k_{app}} \approx 100\% - \frac{k_{\text{EDTA-2Na}}}{k_{app}} \quad (8)$$

$$R_{\cdot\text{O}_2^-} = \frac{k_{\cdot\text{O}_2^-}}{k_{app}} \approx 100\% - \frac{k_{p-BQ}}{k_{app}} \quad (9)$$

$$R_{^1\text{O}_2} = \frac{k_{^1\text{O}_2}}{k_{app}} \approx 100\% - \frac{k_{\text{FFA}}}{k_{app}} \quad (10)$$

3.4. ATZ degradation pathway

To understand the behavior of each atom in ATZ during photocatalysis, the DFT calculation on the ATZ molecule was applied to predict bond breakage (Fig. 8) [43]. The LUMO and HOMO of ATZ can respectively elucidate the electron deficiency site and electron-rich site (Fig. 8B-C) [87]. Apparently, the nitrogen (6 N) between two branched carbon and the chlorine showed a less electron deficient property, and the electrons are more tend to be accumulated in the triazine ring of the ATZ molecule. To better qualify the reactivity of each atom, the Fukui index of them was therefore calculated (Fig. 8D and Table S2). Fukui function is an effective way to predict the reaction tendency of each atom, where the f value was calculated by electron density differences on an atom between its normal state and with one electron missing and the f^+ value was the electron density differences between the normal state and with one more electron (Eqs. 1–4) [13,14,94]. Theoretically, the higher f^0 , f^+ , and f values of an atom respectively refer to an easier radical attack (by $\cdot\text{OH}$ and $\cdot\text{SO}_4^-$), nucleophilic attack (by $\cdot\text{O}_2^-$), and electrophilic attacks (by $^1\text{O}_2$ and h^+) site [14,27]. Fig. E-G visualized the

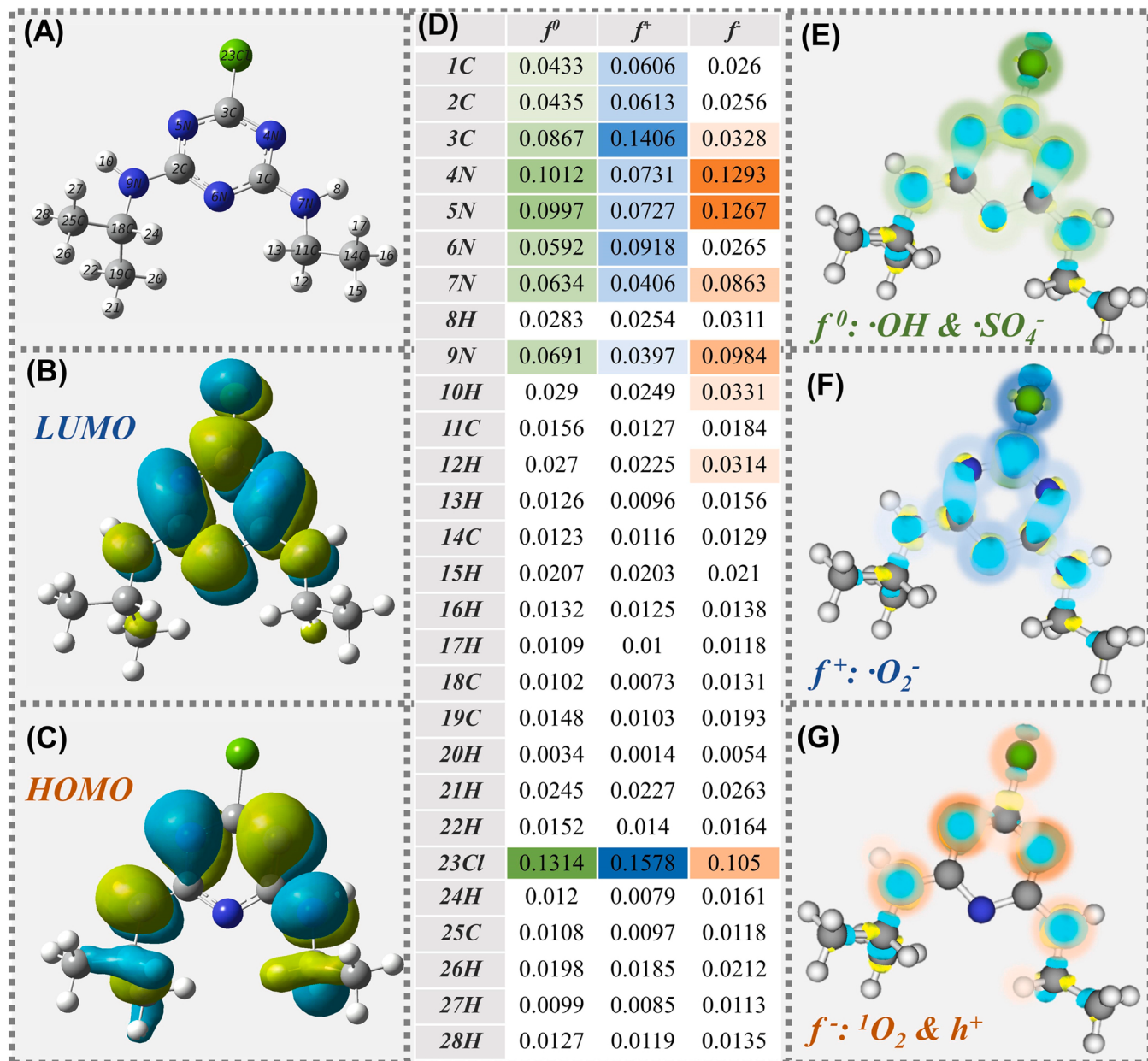


Fig. 8. The Gaussian calculation of ATZ. (A) Atom numbering of ATZ; (B) LUMO and (C) HOMO of ATZ molecule. (D) The calculated Fukui index of each atm in ATZ, (E) f⁰, (F) f⁺, and (G) f⁻ index isosurface on ATZ molecule.

different reactive sites in the ATZ molecule. In general, the triazine ring and the chloride in ATZ are more reactive, no matter for radical, electrophilic, or nucleophilic reactions. This result is in accordance with the atomic reactivity measurement by the CDD value (Table S2 and Fig. S13). Thereinto, the 23Cl, 4 N and 5 N are more likely to be attacked by ·OH and ·SO₄⁻, 23 Cl and 3 C are tend to be nucleophilic attacked, while the 4 N and 5 N atom preferred to be electrophilic attacked. The chloride holds a relatively high reactivity, regardless of the reaction type. While the hydrogen atoms in the side chain are more favorable to react with ¹O₂ and h⁺. Interestingly, such electrophilic reactivity in the side chain can be corresponding to the detection of reactive species: the higher contribution of ¹O₂ may be raised from its ability to destroy the ATZ side chain.

The LC-MS was applied to detect intermediates generated in this system during the ATZ degradation (Fig. 9A and Fig. S14). The ATZ (*m/z* = 216) abundance change detected via LC-MS is following its concentration change measured by HPLC: without the light irradiation and

the PMS activation, the NaCNS shows no influence on ATZ degradation during the 20-min dark reaction, while 95% ATZ can be effectively eliminated after 60 min photocatalytic PMS activation. The information on the main intermediates is summarized in Table S3 according to the *m/z* detected by LC-MS and the previous literature [7,95,96]. The elimination of ATZ in this system mainly produced 11 intermediates, and they can be briefly classified as two degradation paths (pathways A and B) based on their main reaction type (Fig. 9B-C). The intermediate abundance change of major follows a similar tendency. With the generation of abundant reactive species, the abundance of intermediates upsurges rapidly during the first 20 min reaction, along with the rapid degradation of ATZ. During the 20–40 min reaction, the excess reactive species can further degrade these intermediates, their abundance therefore reduced at a certain level, before undergoing a new round of growth at the next 20 min reaction. Specifically, before the reaction, A5 and B5 are already existing in the ATZ solution, which is possibly generated via the hydrolysis of the ATZ molecule [97]. Besides, the

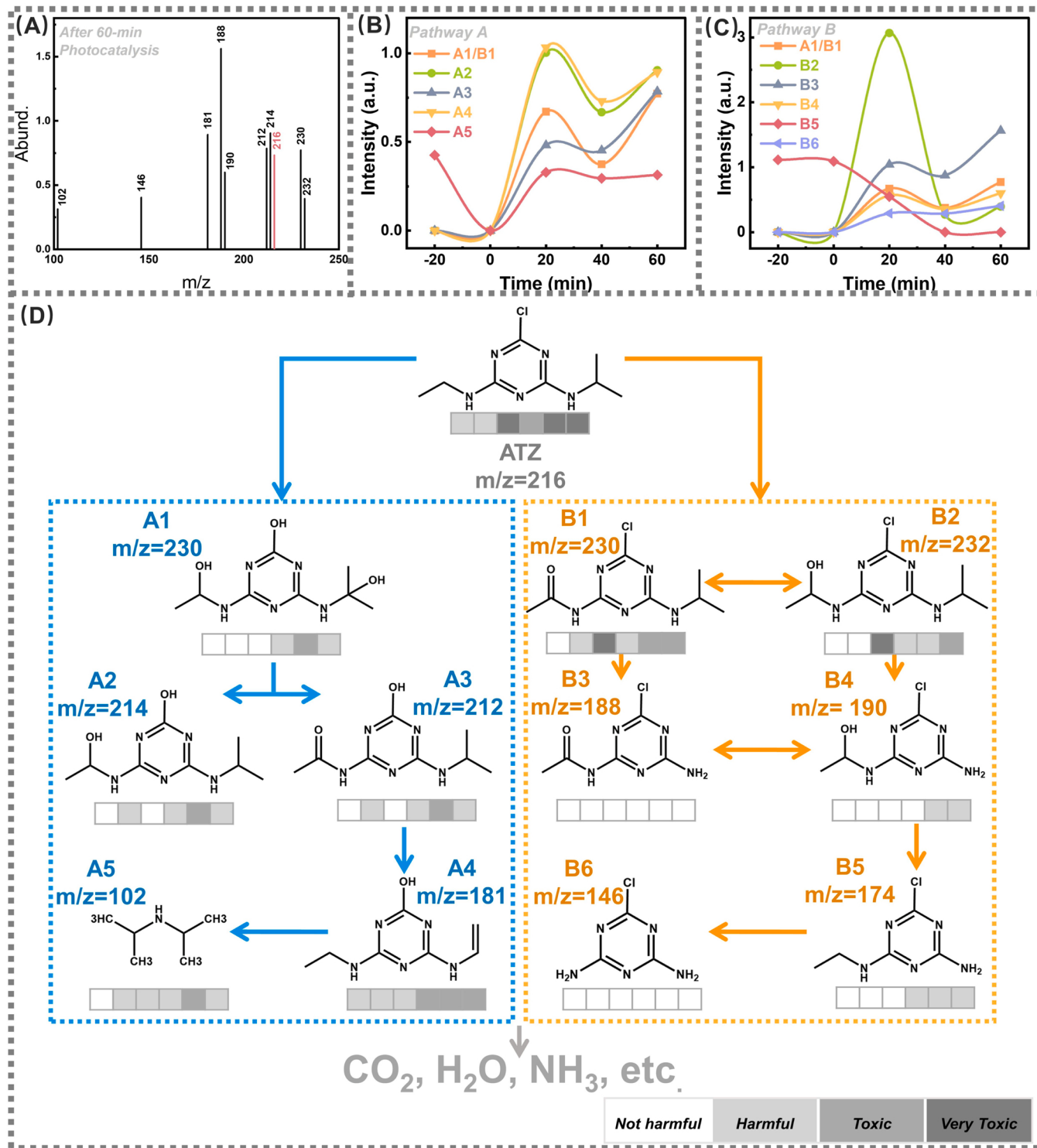


Fig. 9. The degradation path analysis of ATZ. (A) the LC-MS spectra of solution after 60-min photocatalytic PMS activation; the intermediate content change in (B) pathway A and (C) pathway B; (D) the toxicity evolution of intermediates in both degradation pathways estimated via ECOSAR. The six squares with different grey levels below the intermediates respectively refer to their acute toxicity to fish, daphnid, and green algae, and the chronic toxicity of fish, daphnid, and green algae, from left to right.

much higher abundance of B2 at the 20 min than other species can be attributed to its mutual transformation with A2 via dechlorination by oxidation [19].

As predicted by the Fukui index, the chloride in ATZ shows a quiet reactivity. In degradation pathway A of ATZ, its decomposition is mainly originating from the dechlorination, accompanied by the hydroxylation

of the side chain to produce A1. An interconversion possibly occurs in A2 and A3 via addition and elimination reaction, before their further ring-opening reaction. Similarly, though the intermediates in pathway B are not originating from the dechlorination of the triazine ring, the hydrogen atoms on the side chain still are electrophilically attacked and oxidized to the hydroxyl or carbonyl groups, before the demethylation

and deethylation on the triazine-linked nitrogen. To in-depth understand the biological toxicity evolution of the intermediates with the decomposition of ATZ, ECOSAR software was applied (Fig. 9D and Table S4). It was found that the 50% lethal concentration (LC₅₀), term half maximal effective concentration (EC₅₀), and chronic value (ChV) of all the intermediates are higher than pristine ATZ, indicating that the decomposition of ATZ in this system can effectively reduce its ecotoxicity. Based on the United Nations Globally Harmonized System classification, the acute toxicity to fish, daphnid, and green algae, and the chronic toxicity of fish, daphnid, and green algae by different compounds are classified into not harmful, harmful, toxic, and very toxic [98], visualized in Fig. 9D. The toxic level of all the intermediates are effectively decreased. Compared to the chronic toxicity of these intermediates, their reduction in acute toxicity is much more distinct. Interestingly, the overall toxicity of the intermediates generated via pathway B is less harmful than that in pathway A. The B3 and B6 were even not harmful in all the items. Considering the intermediates in different pathways are possibly mutual transformation via dechlorination, and the intermediates would further evolve with the reaction time prolonged, their toxicity of them is expected to further reduce [99].

4. Conclusion

In this work, the NaCNS catalyst was designed to realize the dual modulation on photocarrier separation and activation site, greatly enhanced the ATZ degradation in the photocatalytic PMS activation system. Compared to pristine carbon nitride, from 8.17 to $47.66 \times 10^{-3} \cdot \text{min}^{-1}$. With the effective modification and the optimization of optical coefficient, the reaction rate constants for ATZ degradation by NaCNS-3 in this system dramatically enhanced to $47.66 \times 10^{-3} \cdot \text{min}^{-1}$, which is 5 times higher than the pristine CN. Different from the conventional PMS activation system, the ATZ degradation in this system was mainly dominated by non-radical reactive species $^1\text{O}_2$. This system can maintain efficient ATZ degradation under the interference of most environmental influence factors. According to the Fukui index estimation, the higher contribution rate of $^1\text{O}_2$ for ATZ degradation is possibly originating from its electrophilic attack activity. The ATZ degradation in this system arises the production of 11 major intermediates with lower ecotoxicity, demonstrating effective reduction of the ecotoxicity of this system. Hopefully, this study provides a feasible modulation of catalyst for the sustainable removal of organic pollutants.

CRediT authorship contribution statement

Rongdi Tang: Conceptualization, Validation, Methodology, Investigation, Writing – original draft. **Hao Zeng:** Investigation, Writing – review & editing. **Yaocheng Deng:** Investigation, Funding acquisition, Supervision, Writing - review & editing. **Sheng Xiong:** Investigation, Writing – review & editing. **Ling Li:** Investigation, Writing – review & editing. **Zhanpeng Zhou:** Writing – review & editing. **Jiajia Wang:** Funding acquisition, Writing - review & editing. **Lin Tang:** Supervision, Writing – review & editing, Funding acquisition.

Declaration of Competing Interest

No conflict of interest exists in the submission of this manuscript, and the manuscript has approved by all authors for publication. The authors would like to declare that the manuscript is original and has not been published previously, and is not under consideration for publication elsewhere, in whole or in part.

Data Availability

Data will be made available on request.

Acknowledgment

The study was financially supported by the National Key Research and Development Program of China (No. 2021YFC1910400), the National Natural Science Foundation of China (Grant No. 52270156, 51909089, 52100008), Training Program for Excellent Young Innovators of Changsha (Grant No. kq2209015), and Natural Science Foundation of Hunan Province, China (2021JJ40091).

Appendix A. Supporting information

Supplementary data associated with this article can be found in the online version at doi:10.1016/j.apcatb.2023.122918.

References

- [1] X.X. Fan, F.Q. Song, Bioremediation of atrazine: recent advances and promises, *J. Soils Sed.* 14 (2014) 1727–1737.
- [2] H.J. He, Y.P. Liu, S.H. You, J. Liu, H. Xiao, Z.H. Tu, A review on recent treatment technology for herbicide atrazine in contaminated environment, *Int. J. Environ. Res. Public Health* 16 (2019).
- [3] P.N. Chandra, K. Usha, Removal of atrazine herbicide from water by polyelectrolyte multilayer membranes, *Mater. Today-Proc.* 41 (2021) 622–627.
- [4] Y. Huang, C. Han, Y. Liu, M.N. Nadagouda, L. Machala, K.E. O’Shea, V.K. Sharma, D.D. Dionysiou, Degradation of atrazine by $\text{Zn}_x\text{Cu}_{1-x}\text{Fe}_2\text{O}_4$ nanomaterial-catalyzed sulfate under UV-vis light irradiation: green strategy to generate SO_4^{2-} , *Appl. Catal. B* 221 (2018) 380–392.
- [5] M. Hadei, A. Mesdaghinia, R. Nabizadeh, A.H. Mahvi, S. Rabbani, K. Naddafi, A comprehensive systematic review of photocatalytic degradation of pesticides using nano TiO_2 , *Environ. Sci. Pollut. Res. Int.* 28 (2021) 13055–13071.
- [6] N.X. Chen, D. Valdes, C. Marlin, H. Blanchoud, R. Guerin, M. Rouelle, P. Ribstein, Water, nitrate and atrazine transfer through the unsaturated zone of the Chalk aquifer in northern France, *Sci. Total Environ.* 652 (2019) 927–938.
- [7] R. Tang, D. Gong, Y. Zhou, Y. Deng, C. Feng, S. Xiong, Y. Huang, G. Peng, L. Li, Z. Zhou, Unique g-C₃N₄/PDI-g-C₃N₄ homojunction with synergistic piezo-photocatalytic effect for aquatic contaminant control and H_2O_2 generation under visible light, *Appl. Catal. B* 303 (2022), 120929.
- [8] S.E. Wirbisky, J.L. Freeman, Atrazine exposure and reproductive dysfunction through the hypothalamus-pituitary-gonadal (HPG) axis, *Toxics* 3 (2015) 414–450.
- [9] E. Nyankson, J.K. Efavi, B. Agyei-Tuffour, G. Manu, Synthesis of $\text{TiO}_2\text{-Ag}_2\text{PO}_4$ photocatalyst material with high adsorption capacity and photocatalytic activity: application in the removal of dyes and pesticides, *RSC Adv.* 11 (2021) 17032–17045.
- [10] J. Zhang, X. Wu, X. Zhang, H. Pan, J.E.S. Shearer, H. Zhang, F. Sun, Zn^{2+} -dependent enhancement of Atrazine biodegradation by *Klebsiella variicola* FH-1, *J. Hazard. Mater.* 411 (2021), 125112.
- [11] N. Yang, Y. Liu, J. Zhu, Z. Wang, J. Li, Study on the efficacy and mechanism of $\text{Fe}^{2+}\text{-TiO}_2$ visible heterogeneous Fenton catalytic degradation of atrazine, *Chemosphere* 252 (2020), 126333.
- [12] J.M. Dangwang Dikdim, Y. Gong, G.B. Noumi, J.M. Sieliechi, X. Zhao, N. Ma, M. Yang, J.B. Tchatchueng, Peroxymonosulfate improved photocatalytic degradation of atrazine by activated carbon/graphitic carbon nitride composite under visible light irradiation, *Chemosphere* 217 (2019) 833–842.
- [13] W. Liu, Y. Li, F. Liu, W. Jiang, D. Zhang, J. Liang, Visible-light-driven photocatalytic degradation of diclofenac by carbon quantum dots modified porous g-C₃N₄: Mechanisms, degradation pathway and DFT calculation, *Water Res* 151 (2019) 8–19.
- [14] J. Guo, H. Sun, X. Yuan, L. Jiang, Z. Wu, H. Yu, N. Tang, M. Yu, M. Yan, J. Liang, Photocatalytic degradation of persistent organic pollutants by Co-Cl bond reinforced CoAl-LDH/Bi₂O₃/Cl₂ photocatalyst: mechanism and application prospect evaluation, *Water Res* 219 (2022), 118558.
- [15] P. Shao, J. Tian, F. Yang, X. Duan, S. Gao, W. Shi, X. Luo, F. Cui, S. Luo, S. Wang, Identification and regulation of active sites on nanodiamonds: establishing a highly efficient catalytic system for oxidation of organic contaminants, *Adv. Funct. Mater.* 28 (2018), 1705295.
- [16] X. Chen, J. Yao, H. Dong, M. Hong, N. Gao, Z. Zhang, W. Jiang, Enhanced bezafibrate degradation and power generation via the simultaneous PMS activation in visible light photocatalytic fuel cell, *Water Res* 207 (2021), 117800.
- [17] X. Huang, R. Lei, J. Yuan, F. Gao, C. Jiang, W. Feng, J. Zhuang, P. Liu, Insight into the piezo-photo coupling effect of $\text{PbTiO}_3\text{/CdS}$ composites for piezo-photocatalytic hydrogen production, *Appl. Catal. B* 282 (2021), 119586.
- [18] L. Wang, L. Xie, W. Zhao, S. Liu, Q. Zhao, Oxygen-facilitated dynamic active-site generation on strained MoS₂ during photo-catalytic hydrogen evolution, *Chem. Eng. J.* 405 (2021), 127028.
- [19] R. Tang, D. Gong, Y. Deng, S. Xiong, J. Deng, L. Li, Z. Zhou, J. Zheng, L. Su, L. Yang, $\pi\text{-}\pi$ stacked step-scheme PDI/g-C₃N₄/Ti₃C₂ photocatalyst with enhanced visible photocatalytic degradation towards atrazine via peroxy monosulfate activation, *Chem. Eng. J.* 427 (2022), 131809.
- [20] R.N. Guo, Y.Y. Wang, J.J. Li, X.W. Cheng, D.D. Dionysiou, Sulfamethoxazole degradation by visible light assisted peroxy monosulfate process based on

nanohybrid manganese dioxide incorporating ferric oxide, *Appl. Catal. B-Environ.* 278 (2020).

[21] F. Chen, G.X. Huang, F.B. Yao, Q. Yang, Y.M. Zheng, Q.B. Zhao, H.Q. Yu, Catalytic degradation of ciprofloxacin by a visible-light-assisted peroxymonosulfate activation system: Performance and mechanism, *Water Res.* 173 (2020).

[22] X. Liu, M. Cui, K. Cui, Y. Ding, X. Chen, C. Chen, X. Nie, Construction of Li/K dopants and cyano defects in graphitic carbon nitride for highly efficient peroxymonosulfate activation towards organic contaminants degradation, *Chemosphere* 294 (2022), 133700.

[23] R. Tang, H. Zeng, C. Feng, S. Xiong, L. Li, Z. Zhou, D. Gong, L. Tang, Y. Deng, Twisty C-TiO₂/PCN S-scheme heterojunction with enhanced n- \rightarrow pi* electronic excitation for promoted piezo-photocatalytic effect, *Small* (2023), 2207636.

[24] X. Wang, J. Meng, X. Yang, A. Hu, Y. Yang, Y. Guo, Fabrication of a perylene tetracarboxylic diimide-graphitic carbon nitride heterojunction photocatalyst for efficient degradation of aqueous organic pollutants, *ACS Appl. Mater. Interfaces* 11 (2019) 588–602.

[25] Y. Deng, L. Li, H. Zeng, R. Tang, Z. Zhou, Y. Sun, C. Feng, D. Gong, J. Wang, Y. Huang, Unveiling the origin of high-efficiency charge transport effect of C₃N₅/C₃N₄ heterojunction for activating peroxymonosulfate to degrade atrazine under visible light, *Chem. Eng. J.* 457 (2023), 141261.

[26] F. Chen, L.L. Liu, J.J. Chen, W.W. Li, Y.P. Chen, Y.J. Zhang, J.H. Wu, S.C. Mei, Q. Yang, H.Q. Yu, Efficient decontamination of organic pollutants under high salinity conditions by a nonradical peroxymonosulfate activation system, *Water Res.* 191 (2021), 116799.

[27] N. Li, R. Li, X. Duan, B. Yan, W. Liu, Z. Cheng, G. Chen, L. Hou, S. Wang, Correlation of active sites to generated reactive species and degradation routes of organics in peroxymonosulfate activation by co-loaded carbon, *Environ. Sci. Technol.* 55 (2021) 16163–16174.

[28] S. Xiong, H. Zeng, Y. Deng, C. Feng, R. Tang, Z. Zhou, L. Li, J. Wang, D. Gong, Insights into the dual Z-scheme and piezoelectricity co-driven photocatalyst for ultra-speed degradation of nitenpyram, *Chem. Eng. J.* 451 (2023), 138399.

[29] Y. Deng, Z. Zhou, H. Zeng, R. Tang, L. Li, J. Wang, C. Feng, D. Gong, L. Tang, Y. Huang, Phosphorus and potassium co-doped g-C₃N₄ with multiple-locus synergies to degrade atrazine: Insights into the depth analysis of the generation and role of singlet oxygen, *Appl. Catal. B* 320 (2023), 121942.

[30] C. Feng, L. Tang, Y. Deng, J. Wang, J. Luo, Y. Liu, X. Ouyang, H. Yang, J. Yu, J. Wang, Synthesis of leaf-vein-like g-C₃N₄ with tunable band structures and charge transfer properties for selective photocatalytic H₂O₂ evolution, *Adv. Funct. Mater.* 30 (2020), 2001922.

[31] C. Li, H. Wu, D. Zhu, T. Zhou, M. Yan, G. Chen, J. Sun, G. Dai, F. Ge, H. Dong, High-efficient charge separation driven directionally by pyridine rings grafted on carbon nitride edge for boosting photocatalytic hydrogen evolution, *Appl. Catal. B* 297 (2021), 120433.

[32] P. Kumar, E. Vahidzadeh, U.K. Thakur, P. Kar, K.M. Alam, A. Goswami, N. Mahdi, K. Cui, G.M. Bernard, V.K. Michaelis, K. Shankar, C₃N₅: a low bandgap semiconductor containing an a-linked carbon nitride framework for photocatalytic, photovoltaic and adsorbent applications, *J. Am. Chem. Soc.* 141 (2019) 5415–5436.

[33] R. Tang, H. Zeng, D. Gong, Y. Deng, S. Xiong, L. Li, Z. Zhou, J. Wang, C. Feng, L. Tang, Thin-walled vesicular Triazole-CN-PDI with electronic n- \rightarrow pi* excitation and directional movement for enhanced atrazine photodegradation, *Chem. Eng. J.* 451 (2023), 138445.

[34] G. Wang, R. Huang, J. Zhang, J. Mao, D. Wang, Y. Li, Synergistic modulation of the separation of photo-generated carries via engineering of dual atomic sites for promoting photocatalytic performance, *Adv. Mater.* (2021), e2105904.

[35] H. Zeng, Y. Cheng, E. Repo, X. Yu, X. Xing, T. Zhang, X. Zhao, Trace Iron as single-electron shuttle for interdependent activation of peroxydisulfate and HSO₅⁻/O₂ enables accelerated generation of radicals, *Water Res.* 223 (2022), 118935.

[36] L. Li, X. Yuan, Z. Zhou, R. Tang, Y. Deng, Y. Huang, S. Xiong, L. Su, J. Zhao, D. Gong, Research progress of photocatalytic activated persulfate removal of environmental organic pollutants by metal and nonmetal based photocatalysts, *J. Clean. Prod.* (2022), 133420.

[37] F. Guo, S. Li, Y. Hou, J. Xu, S. Lin, X. Wang, Metalated carbon nitrides as base catalysts for efficient catalytic hydrolysis of carbonyl sulfide, *Chem. Commun. (Camb.)* 55 (2019) 11259–11262.

[38] X. Guo, C. Bartholomew, W. Hecker, L.L. Baxter, Effects of sulfate species on V₂O₅/TiO₂ SCR catalysts in coal and biomass-fired systems, *Appl. Catal. B* 92 (2009) 30–40.

[39] F. Guo, B. Hu, C. Yang, J. Zhang, Y. Hou, X. Wang, On-surface polymerization of in-plane highly ordered carbon nitride nanosheets toward photocatalytic mineralization of mercaptan gas, *Adv. Mater.* 33 (2021), e2101466.

[40] H. Yu, H. Ma, X. Wu, X. Wang, J. Fan, J. Yu, One-step realization of crystallization and cyano-group generation for g-C₃N₄ photocatalysts with Improved H₂ production, *Sol. Rrl* 5 (2020), 2000372.

[41] M. Liu, C. Wei, H. Zhuzhang, J. Zhou, Z. Pan, W. Lin, Z. Yu, G. Zhang, X. Wang, Fully condensed poly (triazine imide) crystals: Extended pi-conjugation and structural defects for overall water splitting, *Angew. Chem.* 61 (2021), e202113389.

[42] G. Zhang, G. Li, T. Heil, S. Zafeiratos, F. Lai, A. Savateev, M. Antonietti, X. Wang, Tailoring the grain boundary chemistry of polymeric carbon nitride for enhanced solar hydrogen production and CO₂ reduction, *Angew. Chem. Int. Ed. Engl.* 58 (2019) 3433–3437.

[43] T. Lu, F. Chen, Multiwin: a multifunctional wavefunction analyzer, *J. Comput. Chem.* 33 (2012) 580–592.

[44] P.W. Ayers, M. Levy, Density functional approach to the frontier-electron theory of chemical reactivity, *Theor. Chem. Acc.* 103 (2000) 353–360.

[45] C. Morell, A. Grand, A. Toro-Labbe, New dual descriptor for chemical reactivity, *J. Phys. Chem. A* 109 (2005) 205–212.

[46] M. Misra, S.R. Chowdhury, T.I. Lee, Sunlight driven decomposition of toxic organic compound, coumarin, p-nitrophenol, and photo reduction of Cr(VI) ions, using a bridge structure of Au@CNT@TiO₂ nanocomposite, *Appl. Catal. B* 272 (2020), 118991.

[47] A. Murphy, Band-gap determination from diffuse reflectance measurements of semiconductor films, and application to photoelectrochemical water-splitting, *Sol. Energy Mater. Sol. Cells* 91 (2007) 1326–1337.

[48] R. Acosta-Herazo, M.A. Mueses, G. Li Puma, F. Machuca-Martinez, Impact of photocatalyst optical properties on the efficiency of solar photocatalytic reactors rationalized by the concepts of initial rate of photon absorption (IRPA) dimensionless boundary layer of photon absorption and apparent optical thickness, *Chem. Eng. J.* 356 (2019) 839–849.

[49] R. Acosta-Herazo, J. Monterroza-Romero, M.A. Mueses, F. Machuca-Martinez, G. Li Puma, Coupling the six flux absorption-scattering model to the heneyey-greenstein scattering phase function: evaluation and optimization of radiation absorption in solar heterogeneous photoreactors, *Chem. Eng. J.* 302 (2016) 86–96.

[50] L. Chen, C. Chen, Z. Yang, S. Li, C. Chu, B. Chen, Simultaneously tuning band structure and oxygen reduction pathway toward high-efficient photocatalytic hydrogen peroxide production using cyano-rich graphitic carbon nitride, *Adv. Funct. Mater.* 31 (2021), 2105731.

[51] Z. Zhu, H. Yin, Y. Wang, C.H. Chuang, L. Xing, M. Dong, Y.R. Lu, G. Casillas-Garcia, Y. Zheng, S. Chen, Y. Dou, P. Liu, Q. Cheng, H. Zhao, Coexisting single-atomic Fe and Ni sites on hierarchically ordered porous carbon as a highly efficient ORR electrocatalyst, *Adv. Mater.* 32 (2020), e2004670.

[52] M. Qiao, Y. Wang, Q. Wang, G. Hu, X. Mamat, S. Zhang, S. Wang, Hierarchically ordered porous carbon with atomically dispersed FeN₄ for ultraefficient oxygen reduction reaction in proton-exchange membrane fuel cells, *Angew. Chem. Int. Ed. Engl.* 59 (2020) 2688–2694.

[53] K. Wang, Q. Li, B. Liu, B. Cheng, W. Ho, J. Yu, Sulfur-doped g-C₃N₄ with enhanced photocatalytic CO₂-reduction performance, *Appl. Catal. B* 176–177 (2015) 44–52.

[54] L. Lin, H. Ou, Y. Zhang, X. Wang, Tri-s-triazine-based crystalline graphitic carbon nitrides for highly efficient hydrogen evolution photocatalysis, *ACS Catal.* 6 (2016) 3921–3931.

[55] H. Yu, R. Shi, Y. Zhao, T. Bian, Y. Zhao, C. Zhou, G.I.N. Waterhouse, L.Z. Wu, C. H. Tung, T. Zhang, Alkali-assisted synthesis of nitrogen deficient graphitic carbon nitride with tunable band structures for efficient visible-light-driven hydrogen evolution, *Adv. Mater.* 29 (2017).

[56] X. Ma, Y. Lv, J. Xu, Y. Liu, R. Zhang, Y. Zhu, A strategy of enhancing the photoactivity of g-C₃N₄ via doping of nonmetal elements: a first-principles study, *J. Phys. Chem. C* 116 (2012) 23485–23493.

[57] M. Sayed, B.C. Zhu, P.Y. Kuang, X.Y. Liu, B. Cheng, A.A. Al Ghamdi, S. Wageh, L. Y. Zhang, J.G. Yu, EPR investigation on electron transfer of 2D/3D g-C₃N₄/ZnO S-scheme heterojunction for enhanced CO₂ photoreduction, *Adv. Sustain Syst.* 6 (2022).

[58] G. Zhang, M. Zhang, X. Ye, X. Qiu, S. Lin, X. Wang, Iodine modified carbon nitride semiconductors as visible light photocatalysts for hydrogen evolution, *Adv. Mater.* 26 (2014) 805–809.

[59] P. Zhang, Y. Tong, Y. Liu, J.J.M. Vequizo, H. Sun, C. Yang, A. Yamakata, F. Fan, W. Lin, X. Wang, W. Choi, Heteroatom dopants promote two-electron O₂ reduction for photocatalytic production of H₂O₂ on polymeric carbon nitride, *Angew. Chem. Int. Ed. Engl.* 59 (2020) 16209–16217.

[60] M.A. Mohamed, M.F.M. Zain, L. Jeffery Minggu, M.B. Kassim, N.A. Saidina Amin, W.N.W. Salleh, M.N.I. Salehmin, M.F. Md Nasir, Z.A. Mohd Hir, Constructing biotemplated 3D porous microtubular C-doped g-C₃N₄ with tunable band structure and enhanced charge carrier separation, *Appl. Catal. B* 236 (2018) 265–279.

[61] S. Zhang, L. Ma, W. Ma, L. Chen, K. Gao, S. Yu, M. Zhang, L. Zhang, G. He, Selenovilogen-appendant metallacycles with highly stable radical cations and long-lived charge separation states for electrochromism and photocatalysis, *Angew. Chem. Int. Ed. Engl.* 61 (2022), e202209054.

[62] J. Han, Z. Zhu, N. Li, D. Chen, Q. Xu, H. Li, J. He, J. Lu, Metalloporphyrin-based D-type conjugated organic polymer nanotube for efficient photocatalytic degradation, *Appl. Catal. B* 291 (2021), 120108.

[63] C. Feng, L. Tang, Y. Deng, J. Wang, Y. Liu, X. Ouyang, H. Yang, J. Yu, J. Wang, A novel sulfur-assisted annealing method of g-C₃N₄ nanosheets compensates for the loss of light absorption with further promoted charge transfer for photocatalytic production of H₂ and H₂O₂, *Appl. Catal. B* 281 (2021), 119539.

[64] W. Fang, J. Liu, L. Yu, Z. Jiang, W. Shangguan, Novel (Na, O) co-doped g-C₃N₄ with simultaneously enhanced absorption and narrowed bandgap for highly efficient hydrogen evolution, *Appl. Catal. B* 209 (2017) 631–636.

[65] J. Zhang, S. Hu, Y. Wang, A convenient method to prepare a novel alkali metal sodium doped carbon nitride photocatalyst with a tunable band structure, *RSC Adv.* 4 (2014) 62912–62919.

[66] X. Lin, H. Du, D. Jiang, P. Zhang, Z. Yu, H. Bi, Y. Yuan, Microwave awakening the n- \rightarrow pi* electronic transition in highly crystalline polymeric carbon nitride nanosheets for photocatalytic hydrogen generation, *J. Energy Chem.* 65 (2022) 541–547.

[67] Y. Chen, B. Wang, S. Lin, Y. Zhang, X. Wang, Activation of n- \rightarrow pi* transitions in two-dimensional conjugated polymers for visible light photocatalysis, *J. Phys. Chem. C* 118 (2014) 29981–29989.

[68] G.G. Zhang, G.S. Li, Z.A. Lan, L.H. Lin, A. Savateev, T. Heil, S. Zafeiratos, X. C. Wang, M. Antonietti, Optimizing optical absorption, exciton dissociation, and charge transfer of a polymeric carbon nitride with ultrahigh solar hydrogen production activity, *Angew. Chem. Int. Ed.* 56 (2017) 13445–13449.

[69] Y. Deng, L. Tang, G. Zeng, Z. Zhu, M. Yan, Y. Zhou, J. Wang, Y. Liu, J. Wang, Insight into highly efficient simultaneous photocatalytic removal of Cr(VI) and 2,4-

dichlorophenol under visible light irradiation by phosphorus doped porous ultrathin g-C₃N₄ nanosheets from aqueous media: Performance and reaction mechanism, *Appl. Catal. B* 203 (2017) 343–354.

[70] Y. Deng, L. Tang, C. Feng, G. Zeng, Z. Chen, J. Wang, H. Feng, B. Peng, Y. Liu, Y. Zhou, Insight into the dual-channel charge-charrier transfer path for nonmetal plasmonic tungsten oxide based composites with boosted photocatalytic activity under full-spectrum light, *Appl. Catal. B* 235 (2018) 225–237.

[71] G. Liu, P. Niu, C. Sun, S.C. Smith, Z. Chen, G.Q. Lu, H.M. Cheng, Unique electronic structure induced high photoreactivity of sulfur-doped graphitic C₃N₄, *J. Am. Chem. Soc.* 132 (2010) 11642–11648.

[72] G. Zhao, J. Ding, J. Ren, Q. Zhao, Q. Gao, K. Wang, L. Wei, X. Chen, F. Zhou, D. Dionysiou, Insight into the visible light activation of sulfite by Fe/g-C₃N₄ with rich N vacancies for pollutant removal and sterilization: a novel approach for enhanced generation of oxysulfur radical, *Chem. Eng. J.* 438 (2022), 135663.

[73] X. Han, L. An, Y. Hu, Y. Li, C. Hou, H. Wang, Q. Zhang, Ti₃C₂ MXene-derived carbon-doped TiO₂ coupled with g-C₃N₄ as the visible-light photocatalysts for photocatalytic H₂ generation, *Appl. Catal. B* 265 (2020), 118539.

[74] R. Tang, D. Gong, Y. Deng, S. Xiong, J. Zheng, L. Li, Z. Zhou, L. Su, J. Zhao, pi-pi stacking derived from graphene-like biochar/g-C₃N₄ with tunable band structure for photocatalytic antibiotics degradation via peroxymonosulfate activation, *J. Hazard. Mater.* 423 (2022), 126944.

[75] E.M. Samsudin, S.B. Abd Hamid, J.C. Juan, W.J. Basirun, A.E. Kandjani, S. K. Bhargava, Controlled nitrogen insertion in titanium dioxide for optimal photocatalytic degradation of atrazine, *RSC Adv.* 5 (2015) 44041–44052.

[76] T.S. Jamil, H.A. Abbas, R.A. Nasr, R.N. Vannier, Visible light activity of BaFe_{1-x}Cu_xO_{3-δ} as photocatalyst for atrazine degradation, *Ecotoxicol. Environ. Saf.* 163 (2018) 620–628.

[77] H.X. Wang, L.N. Zhu, F.Q. Guo, Photoelectrocatalytic degradation of atrazine by boron-fluorine Co-doped TiO₂ nanotube arrays, *Environ. Sci. Pollut. Res. Int.* 26 (2019) 33847–33855.

[78] M.L. Yola, T. Eren, N. Atar, A novel efficient photocatalyst based on TiO₂ nanoparticles involved boron enrichment waste for photocatalytic degradation of atrazine, *Chem. Eng. J.* 250 (2014) 288–294.

[79] S. Klementova, M. Zlamal, Photochemical degradation of triazine herbicides - comparison of homogeneous and heterogeneous photocatalysis, *Photochem. Photobiol. Sci.* 12 (2013) 660–663.

[80] S.H. Ho, Y.D. Chen, R. Li, C. Zhang, Y. Ge, G. Cao, M. Ma, X. Duan, S. Wang, N. Q. Ren, N-doped graphitic biochar from C-phycocyanin extracted Spirulina residue for catalytic persulfate activation toward nonradical disinfection and organic oxidation, *Water Res* 159 (2019) 77–86.

[81] H. Wang, Y. Sun, Y. Wu, W. Tu, S. Wu, X. Yuan, G. Zeng, Z.J. Xu, S. Li, J.W. Chew, Electrical promotion of spatially photoinduced charge separation via interfacial-built-in quasi-alloying effect in hierarchical Zn₂In₂S₅/Ti₃C₂(O, OH)_x hybrids toward efficient photocatalytic hydrogen evolution and environmental remediation, *Appl. Catal. B* 245 (2019) 290–301.

[82] Q. Wu, Y. Zhang, H. Liu, H. Liu, J. Tao, M.H. Cui, Z. Zheng, D. Wen, X. Zhan, Fe_xN produced in pharmaceutical sludge biochar by endogenous Fe and exogenous N doping to enhance peroxymonosulfate activation for levofloxacin degradation, *Water Res* 224 (2022), 119022.

[83] M. Li, Y.T. Jin, D.Y. Cao, L.L. Yang, J.F. Yan, Z.X. Zhang, Z. Liu, L.W. Huang, S. Q. Zhou, J.L. Cheng, Q. Zhao, H.M. Zhao, N.X. Feng, C.H. Mo, Efficient decomposition of perfluorooctane sulfonate by electrochemical activation of peroxymonosulfate in aqueous solution: efficacy, reaction mechanism, active sites, and application potential, *Water Res* 221 (2022), 118778.

[84] C. Ding, G. Zeng, Y. Tao, X. Long, D. Gong, N. Zhou, R. Zeng, X. Liu, Y. Deng, M. E. Zhong, Environmental-friendly hydrochar-montmorillonite composite for efficient catalytic degradation of dicamba and alleviating its damage to crops, *Sci. Total Environ.* 856 (2022), 158917.

[85] J. Wang, S. Wang, Activation of persulfate (PS) and peroxymonosulfate (PMS) and application for the degradation of emerging contaminants, *Chem. Eng. J.* 334 (2018) 1502–1517.

[86] N.S. Shah, X.X. He, H.M. Khan, J.A. Khan, K.E. O'Shea, D.L. Boccelli, D. Dionysiou, Efficient removal of endosulfan from aqueous solution by UV-C/ peroxides: A comparative study, *J. Hazard. Mater.* 263 (2013) 584–592.

[87] Y.X. He, J. Qian, P.F. Wang, J. Wu, B.H. Lu, S.J. Tang, P. Gao, Acceleration of levofloxacin degradation by combination of multiple free radicals via MoS₂ anchored in manganese ferrite doped perovskite activated PMS under visible light, *Chem. Eng. J.* 431 (2022).

[88] Y.H. Guan, J. Ma, Y.M. Ren, Y.L. Liu, J.Y. Xiao, L.Q. Lin, C. Zhang, Efficient degradation of atrazine by magnetic porous copper ferrite catalyzed peroxymonosulfate oxidation via the formation of hydroxyl and sulfate radicals, *Water Res* 47 (2013) 5431–5438.

[89] J. Huang, Z. Zhou, M. Ali, X. Gu, M. Danish, Q. Sui, S. Lyu, Degradation of trichloroethene by citric acid chelated Fe(II) catalyzing sodium percarbonate in the environment of sodium dodecyl sulfate aqueous solution, *Chemosphere* 281 (2021), 130798.

[90] T. Maqbool, J. Zhang, Y. Qin, M. Bilal Asif, Q. Viet Ly, Z. Zhang, Fluorescence moieties as a surrogate for residual chlorine in three drinking water networks, *Chem. Eng. J.* 411 (2021), 128519.

[91] J.C.G. Sousa, A.R. Ribeiro, M.O. Barbosa, M.F.R. Pereira, A.M.T. Silva, A review on environmental monitoring of water organic pollutants identified by EU guidelines, *J. Hazard. Mater.* 344 (2018) 146–162.

[92] H. Ming, P. Zhang, Y. Yang, Y. Zou, C. Yang, Y. Hou, K. Ding, J. Zhang, X. Wang, Tailored poly-heptazine units in carbon nitride for activating peroxymonosulfate to degrade organic contaminants with visible light, *Appl. Catal. B* 311 (2022), 121341.

[93] X. Zhou, Z. Yang, Y. Chen, H. Feng, J. Yu, J. Tang, X. Ren, J. Tang, J. Wang, L. Tang, Single-atom Ru loaded on layered double hydroxide catalyzes peroxymonosulfate for effective E. coli inactivation via a non-radical pathway: efficiency and mechanism, *J. Hazard. Mater.* 440 (2022), 129720.

[94] C. Liu, S. Mao, M. Shi, F. Wang, M. Xia, Q. Chen, X. Ju, Peroxymonosulfate activation through 2D/2D Z-scheme CoAl-LDH/BiOBr photocatalyst under visible light for ciprofloxacin degradation, *J. Hazard. Mater.* 420 (2021), 126613.

[95] Y. Gao, Y. Zhou, S.Y. Pang, J. Jiang, Y.M. Shen, Y. Song, J.B. Duan, Q. Guo, Enhanced peroxymonosulfate activation via complexed Mn(II): a novel non-radical oxidation mechanism involving manganese intermediates, *Water Res.* 193 (2021), 116856.

[96] S.Q. Tian, J.Y. Qi, Y.P. Wang, Y.L. Liu, L. Wang, J. Ma, Heterogeneous catalytic ozonation of atrazine with Mn-loaded and Fe-loaded biochar, *Water Res.* 193 (2021), 116860.

[97] J. Li, J. Hu, W. Xu, M. Ling, J. Yao, Hydrolysis reaction mechanism in atrazine metabolism and prediction of its metabolites' toxicities, *J. Agric. Food Chem.* 62 (2014) 4852–4863.

[98] L. Zhang, J. Chen, T. Zheng, Y. Xu, T. Liu, W. Yin, Y. Zhang, X. Zhou, Co-Mn spinel oxides trigger peracetic acid activation for ultrafast degradation of sulfonamide antibiotics: Unveiling critical role of Mn species in boosting Co activity, *Water Res.* 229 (2022), 119462.

[99] H. Wang, W. Guo, Q. Si, B. Liu, Q. Zhao, H. Luo, N. Ren, Multipath elimination of bisphenol A over bifunctional polymeric carbon nitride/biochar hybrids in the presence of persulfate and visible light, *J. Hazard. Mater.* 417 (2021), 126008.